Sediment damage caused by gas exsolution: A key mechanism for mud volcano formation

Arthur Blouin, Nabil Sultan, Jean-Paul Callot, Patrice Imbert

Sediment damage caused by gas exsolution: a key mechanism for mud volcano formation

Arthur Blouin[1,2,3], Nabil Sultan[1], Jean-Paul Callot[3], Patrice Imbert[2].

1 Ifremer, LAD, géosciences marines, REM, Centre de Bretagne, 29280 Plouzané

2 R&D/EP Total S.A., Avenue Larribau, 64000 Pau

3 CNRS /TOTAL/UNIV PAU & PAYS ADOUR/ E2S UPPA, Laboratoire des Fluides Complexes et leurs Réservoirs-IPRA, UMR5150, 64000, PAU, France

Keywords: consolidation testing; gas exsolution; gassy sediments; sediment damage; mud volcano

Highlights:

- Fracture geometry is controlled by the degree of gas saturation and preconsolidation pressure
- Gas exsolution provokes sediment damage and change in mechanical behavior
- Sediments do not recover their initial behavior completely after reloading
- Gas exsolution is able to generate mud from compacted sediments

Abstract

Gassy sediments are common in marine environments and are characterized by a specific mechanical behavior significantly different from that of water-saturated sediments. It is shown that gas causes damage and initiates fractures in sediments. To define the controlling parameters dominating the damage process during gas exsolution and its consequences in terms of hydro-mechanical behavior, we developed a specific consolidation apparatus to test sediments collected from the active Absheron Mud Volcano. Indeed, mud volcano formation is initiated by gas exsolution and subsequent mud generation at depth from stratified sediments.

Gas was generated in the samples by circulating carbonated water through the fine-grained sediments, then decreasing the total pressure. Particular attention was given to the impact of gas saturation and associated damage and fractures on P-wave velocity, sediment compressibility, permeability and preconsolidation pressure. Results show that fracture geometry is mainly controlled by the degree of gas saturation and preconsolidation pressure. The damage level increases with the degree of gas saturation while the elastic modulus of sediments is degraded. Experimental data show that sediments do not entirely recover their original mechanical behavior when gas dissipates. Finally, the experimental data confirm that gas exsolution and expansion is a key mechanism for mud generation.

1. Introduction

Sediments partially saturated with free gas are a widespread occurrence and are found in varying marine environments (Grozic, *et al.*, 2000). Nageswaran (1983) discriminates between two free-gas distributions: continuous gas phase and discrete separated gas bubbles. The latter is defined as gassy sediments and Nageswaran (1983) gives a maximum limit in terms of the degree of gas saturation ($S_g < 15\%$). Gassy sediments are a well-known issue in marine geotechnics that has been studied for decades as the detection and quantification of free-gas content is essential for geohazard assessment (Esrig & Kirby, 1977; Sobkowicz & Morgenstern, 1984; Thomas, 1987; Sultan, *et al.*, 2004, 2012; Judd & Hovland, 2007; Riboulot, *et al.*, 2013).

The main difficulty when studying gassy fine-grained sediments in laboratory is to obtain a discrete distribution of gas bubbles. Several techniques exist, including the generation of free gas through the zeolite molecular sieve technique (Nageswaran, 1983; Thomas, 1987; Wheeler, 1988; Sills, *et al.*, 1991; Nava Castro, *et al.*, 2013), the generation of biogenic gas through bacteria (Sills & Gonzalez, 2001; Rebata-Landa, *et al.*, 2012) and finally the generation of gas bubbles through the circulation of overpressured carbonated water followed by decompression (Grozic, *et al.*, 2000; Sultan, *et al.*, 2012).

The mechanical behavior of gassy sediments has been extensively studied over the last decades (Thomas, 1987; Wheeler, 1988; Sills, *et al.*, 1991; Helgerud, *et al.*, 1999; Grozic, *et al.*, 2005; Sultan, *et al.*, 2012; Nava Castro, *et al.*, 2013; Jang & Santamarina, 2014). P-wave velocity attenuation is a typical feature of all gassy sediments (Sills, *et al.*, 1991; Helgerud, *et al.*, 1999; Sultan, *et al.*, 2012). Thomas (1987) shows that fine-grained gassy sediments subjected to consolidation behave like a water-saturated soil with discrete compressible solid inclusions modeling the gas bubble compressibility. Moreover, several studies show that the compressible gas bubbles deform under applied stresses causing a delay in the consolidation process and therefore a change in sediment compressibility (Sills, *et al.*, 1991; Grozic, *et al.*, 2005; Nava Castro, *et al.*, 2013; Liu, *et al.*, 2016). Additionally, numerous experiments and numerical simulations show that the presence of discrete gas bubbles that nucleated directly in the sediments decrease its permeability (Egermann & Vizika, 2000; Naylor, *et al.*, 2000; Jang & Santamarina, 2014). Revil *et al.* (1998) even shows that the formation of capillary seals can generate an effective permeability lower than intrinsic sediment permeability. Furthermore, Sultan, *et al.* (2012) show the important drop in preconsolidation pressure proving that fine-grained sediments are damaged after gas exsolution. Finally, Wheeler (1988), Lunne, *et al.* (2001), Hight, *et*

al. (2002), Sultan & Garziglia (2014) and Hong *et al.* (2017) demonstrate that the undrained shear strength of fine-grained gassy sediments is also impacted by the presence of free gas.

Mud volcanoes are one of the most spectacular geological features related to gas venting. Gas, mostly methane and carbon dioxide, is expelled at the seafloor along with a fluid mélange, varying in proportion, of water, fine-grained sediments and larger rock fragments (Kopf, 2002; Mazzini & Etiope, 2017). Mud is commonly sourced from depths of several kilometers (Stewart & Davies, 2006; Kirkham, 2015; Blouin, *et al.*, 2019). The Lusi catastrophe, ongoing since 2006, allowed to monitor mud volcano formation from its initiation (Tingay, *et al.*, 2008, 2017; Mazzini, *et al.*, 2012). Tingay *et al.* (2017) demonstrated that the key parameters of the Lusi triggering were the high overpressure and the gas influx into weak layers. Moreover, Capaccioni *et al.* (2017) show that the emplacement of sand volcanoes during Cone Penetration Testing in Italy was caused by gas exsolution and expansion in loose deposits. Therefore, Tingay *et al.* (2015) and Blouin *et al.* (2019) proposed gas exsolution and expansion triggered by hydrofracturing and the subsequent drop in pore fluid pressure as mud generation mechanisms.

The aim of this study is to identify the impact of gas expansion and exsolution on the mechanical behavior of fine-grained sediments sampled directly on the active Absheron Mud Volcano (AMV - South Caspian Basin; Blouin *et al.*, 2019). Particular attention was given to the gas impact on sediment structure, acoustic properties (P-wave velocity), compressibility and preconsolidation pressure by carrying out a series of consolidation/compressibility tests using a novel experimental set-up. The main questions motivating this work are summarized below:

If gas exsolution within fine-grained sediments is already proven to cause damage (Sultan, *et al.*, 2012), what are the controlling parameters dominating the process and what are the consequences in terms of hydromechanical behavior?

Do the mechanical properties of the sediments recover from gas exsolution/expansion after mechanical reloading?

What are the conditions that allow gas exsolution and expansion in the host sediment to generate mud?

2. Experimental testing

2.1. Properties of tested soil and sample preparation

To identify the potential geohazard of the AMV, Fugro conducted an offshore geotechnical survey in 2014 (Dan & Po, 12/09/2017, pers. com.) including rotary drilling with sediment coring up to 34 meters deep (Figure 1 for location) and in situ CPTu measurements (Cone Penetration Testing, with piezocone; Lunne, 2010; Boggess & Robertson, 2011). These data and cores are used in the present work to characterize the geotechnical properties of the natural and remolded sediments.

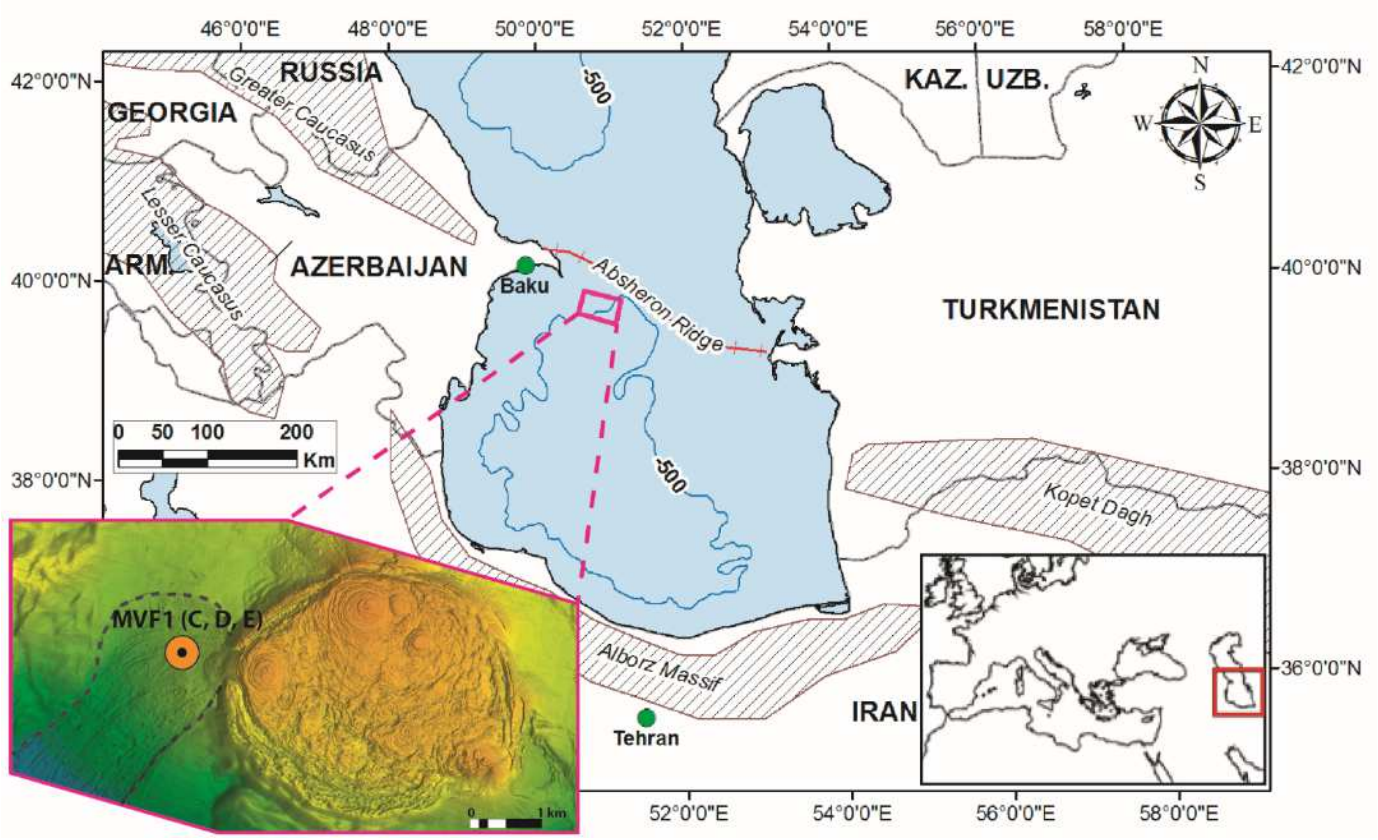

Figure 1: Location of the study area. The Absheron Mud Volcano is located on the Absheron anticline (purple rectangle), 100 km to the SE of Baku, North of the South Caspian Basin. Details of the seafloor morphology of the area surrounding the mud volcano is given in the inset in the bottom left hand corner (read Blouin et al. (2019) for more details). The rotary drilling MVF1, located on the mudflow, is also displayed.

CPTu profiling and sediment type classification acquired at the MVF1 drilling site, on the western mudflow of the AMV (Dan & Po, 12/09/2017, pers. com.) show the presence of three different mechanical intervals. For this study, and in order to carry out basic geotechnical analyses, we selected three samples from the three different intervals (MECA-6, MECA-15 and MECA-22; Table 1).

Grain size distribution was determined with a laser diffraction apparatus (Mastersizer 3000, Ryzak & Bieganowski, 2011). Results show that the three reference samples have roughly the same grain size distribution with

peak values between 4 and 6 µm and a minor signature around 400 µm (Figure 2a). However, the MECA-6 sample is slightly poorer in the fine fraction and richer in the coarser fraction. The d_X is the grain size where X% of the grains are finer. The three samples differentiate on the coarser fraction as their d_{10} and d_{50} are roughly the same (Table 2). Nevertheless, all the samples have a d_{90} greater than 35 µm, meaning that 90% of the particles are smaller than 35 µm. 50% of the mud particles are smaller than 5 µm. Therefore, the studied samples are essentially composed of silts and clay-size particles with a minor fraction of very fine to medium sand.

Core Name	Sample Name	Type of sample	Type of analysis	Water depth (m)	Depth Below Seafloor (m)
MVF1C	MECA-1	Core Sample	Consolidation cell	521	0.3
	MECA-2	Core Sample	Consolidation cell		1.0
	MECA-3	Core Sample	Consolidation cell		2.0
	MECA-4	Core Sample	Consolidation cell		2.2
	MECA-5	Core Sample	Consolidation cell		3.0
	MECA-6	Core Sample	Grain size distribution, oedometer and mineralogy		3.6
	MECA-7	Core Sample	Consolidation cell		4.0
	MECA-8	Core Sample	Consolidation cell		4.8
MVF1D	MECA-15	Core Sample	Grain size distribution, oedometer	522	10.0
MVF1E	MECA-22	Core Sample	Grain size distribution, oedometer and mineralogy	522	33.1
	MECA-23	Core Sample	Consolidation cell		39.6

Table 1: Summary of sample details including water depth, depth below seafloor (BSF) and type of analysis completed on each sample.

A mineralogical analysis was performed on two of the samples used in this study (MECA-6 and MECA-22, see Table 1). Table 2 displays the main mineralogical fractions for the two tested samples grouped into three poles: quartz, clays and calcite. Other mineral types were distributed between the pole according to their density or their mineral group. For instance, the dolomite percentage was added to the calcite pole, and apatite to the clay pole.

The Atterberg limits were determined using the fall cone method (Feng, 2000). Results are presented in Table 2. Sediments from the three samples have a mean plastic limit value of (w_P) 20.3%, a mean liquid limit (w_L) of 43% and a mean plasticity index (PI) of 22.7%.

Oedometer tests were carried out on the same reference samples using incremental loading according to the ASTM D-2435 method (ASTM International, 1996). Three oedometer reference samples were prepared from three

mud samples (MECA-6, MECA-15, MECA-22; Table 1) with a water content of approximately 1.5 the liquid limit (w_L). Compressibility curves during loading and unloading tests are plotted in Figure 2b. The three samples have almost the same virgin consolidation curve with a compression index Cc of 0.3 and a swelling index C_S of 0.08 (Table 2).

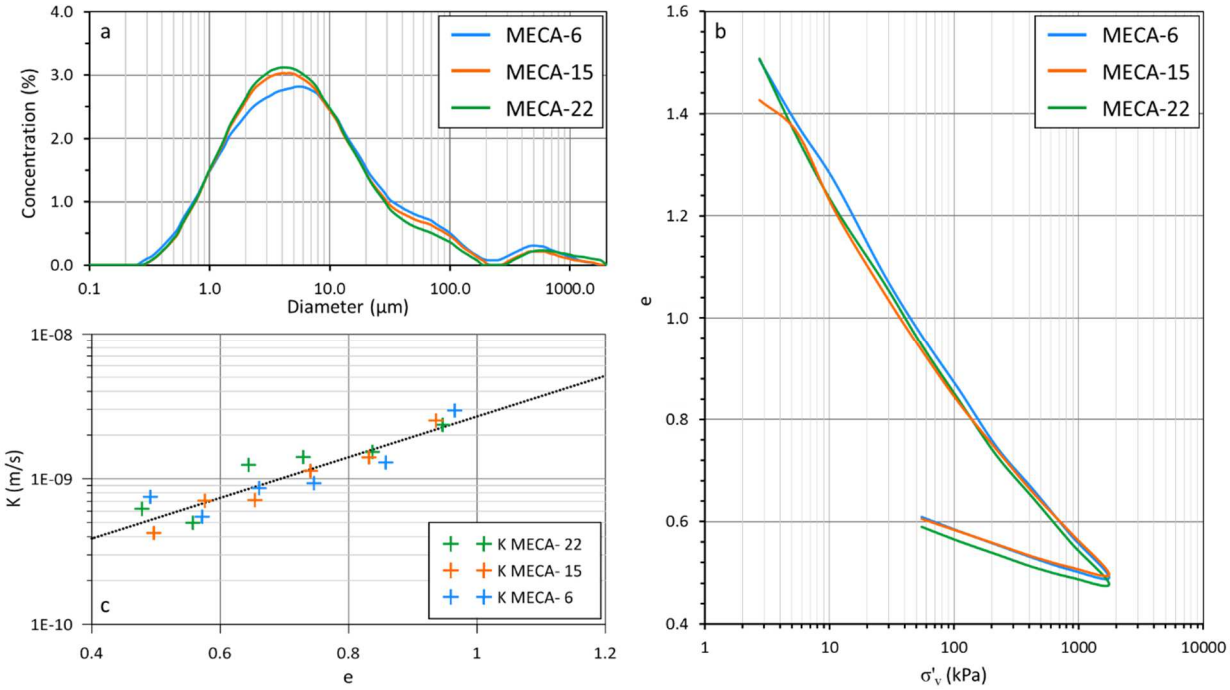

Figure 2: Basic properties of the tested three water-saturated samples. a: grain size distribution. b: oedemeter compressibility and c: hydraulic conductivity versus void ratio.

During consolidation tests, hydraulic conductivity measurements were carried out using the falling-head test method. Figure 2c summarizes the results as a cross-plot of hydraulic conductivity versus void ratio. The three samples have a similar trend and hydraulic conductivity K stands between 8.10^{-8} and 7.10^{-9} m/s for void ratios between 1 and 0.4. Skempton (1944) gives an empirical expression linking the compression index and the liquid limit of remolded clays. Using the mean liquid limit of the tested sediment, the calculated Cc is 0.32, which agrees with values obtained using oedometer tests (Table 2).

Due to the insignificant variability of the basic properties of the three tested samples, eight other samples were selected from the same three intervals of the MVF1 core in order to test the impact of gas exsolution using the new experimental apparatus developed in the present study (Table 1). To obtain homogeneous samples, the eight samples were mixed and remolded with a water content of approximately twice the liquid limit (Table 2). Remolding was carried out using a mechanical stirrer. The same slurry was used in all the tests presented in the paper. At the end of each test, a small part of the tested sample served to measure the final water content.

	MECA-6	MECA-15	MECA-22
d_{10} (µm)	1.17	1.22	1.21
d_{50} (µm)	5.91	5.41	5.23
d_{90} (µm)	53.7	42.9	36.8
w_P (%)	21.0	23.0	17.0
w_L (%)	42.0	43.0	44.0
PI	21.0	20.0	27.0
C_C	0.32	0.29	0.31
C_S	0.08	0.07	0.07
mass% Quartz	38.5		36
mass% Clays	51.5		55.5
mass% Calcite	10		8.5

Table 2: Synthesis of the main sample properties. Further details are given in Figure 2.

2.2. Experimental set-up and calibration

In order to analyze the gassy sediments, we developed a novel experimental set-up, composed of three main modules (Figure 3): the consolidation cell and the mechanical press, designed to apply vertical loads, and the saturation module where water is carbonated under a given CO_2 gas pressure. The last module is the control panel that connects all the experimental set-up sensors with a computer in order to constrain and record the different parameters.

The consolidation cell is composed of a Plexiglas cylinder that forms, along the two end covers, the fixed part of the system (Figure 3). The type of Plexiglas used for the consolidation cell is PMMA XT, which has an elastic modulus of 3.3 GPa and a yield stress of 70-80 MPa. The Plexiglas cylinder is 15 mm thick. The piston is composed of a steel rod fixed into a pierced plastic cylinder (Figure 3). Two porous stones placed on the top and the bottom of the sample ensure the consolidation of the sediment during loading. A load cell and a vertical displacement sensor allow controlling the rate of displacement and the axial force applied to the sample (Figure 3). The load cell is limited to 5 kN (≈1300 kPa considering the sample section) with a precision of ± 0.005 kN. A bender element system (supplied by GDS Ltd, UK; Hasan and Wheeler (2015)) is integrated into the piston and the bottom pedestal to measure P-wave velocity (Figure 3).

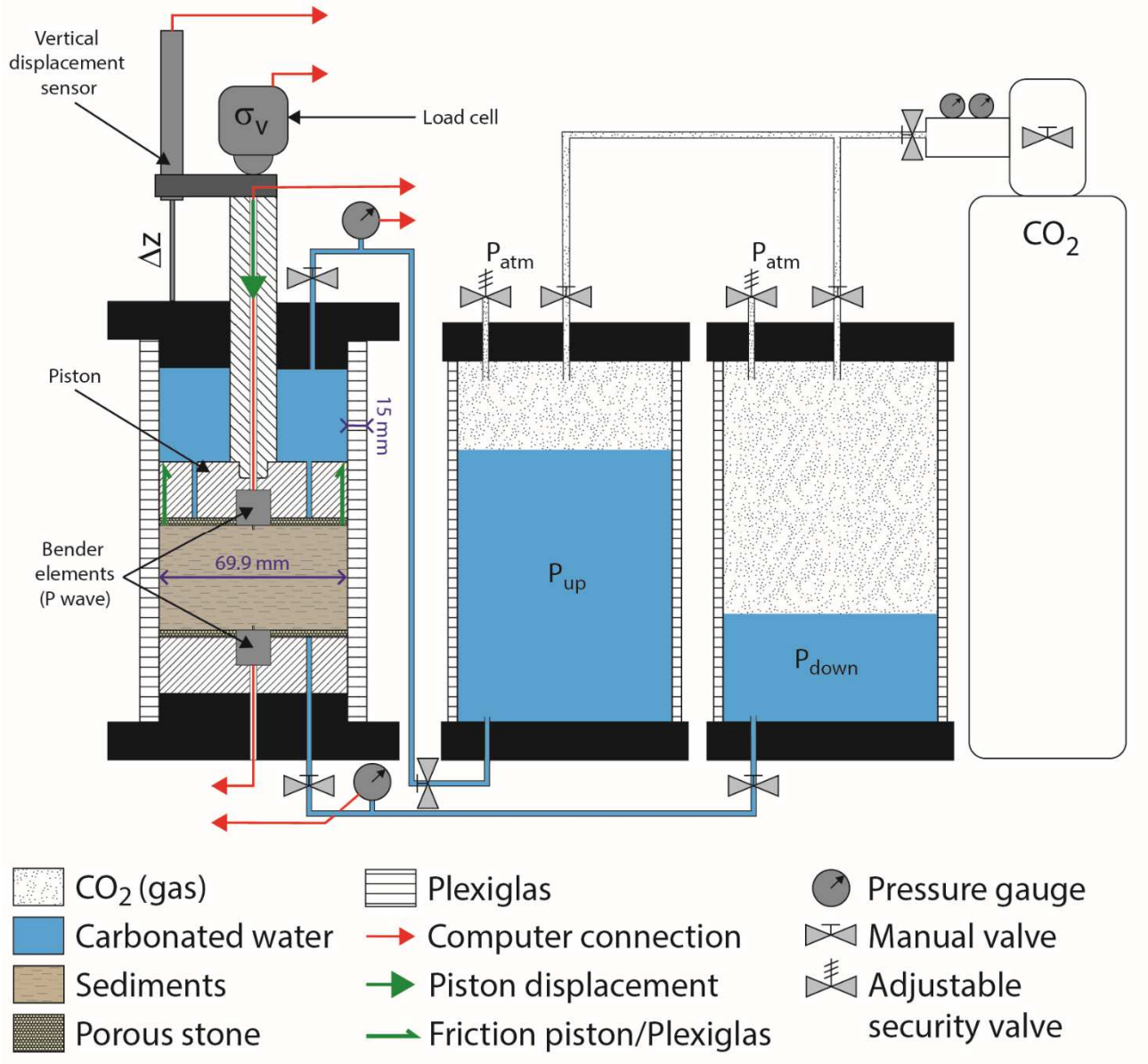

Figure 3: Detailed experimental setup showing the consolidation cell, the saturation system and the main sensors emplacement. Green arrows indicate the orientation of friction forces for a downward motion of the piston.

A lip seal circles the piston and avoids sediments flowing above the piston but generates a non-negligible friction on the inner surface of the Plexiglas cylinder. This friction is measured by the load cell and is calibrated to properly calculate the net applied vertical effective stress. Force balance at the sediment-piston contact shows that the measured force is a composition of the friction, a vertical upload force due to the different piston surfaces on which fluid pressure is applied (Figure 3), and the net applied load. Friction is always opposed to piston movement.

The lip seal is asymmetrical. Therefore, calibration of friction must be made during loading and unloading (Figure 4). To do so, the consolidation cell was filled with water and underwent different load and unload cycles at different pore water pressures. The piston velocity used in the different calibration tests is the same in the rest of our testing program: 0.12 mm/h during loading, 0.5 mm/h during unloading. The load velocity was determined by

comparing the oedometer compressibility curve (Figure 2) to the compressibility one using the present advanced consolidation cell.

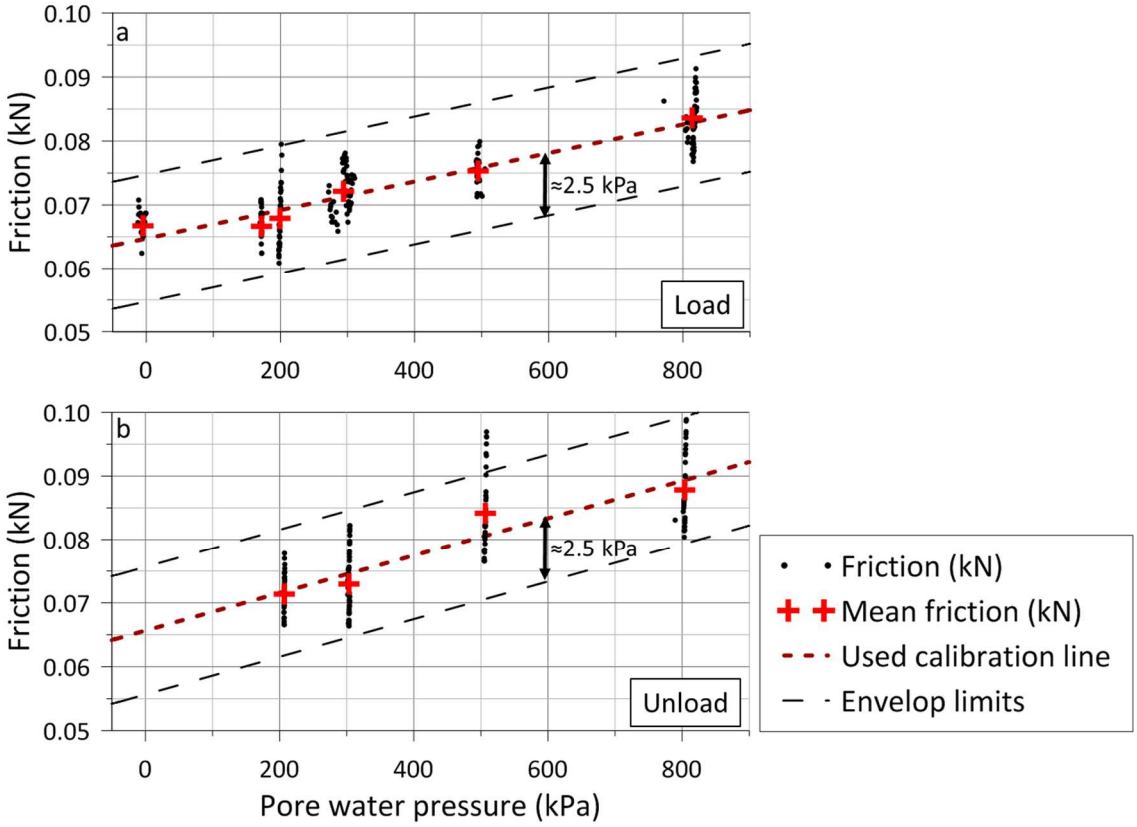

Figure 4: friction calibration during (a) loading and (b) unloading for different pore water pressures. The dotted black lines correspond to the envelop values of friction. The friction variation is within ± 2.5 kPa.

The results show that the friction is a linear function of pressure and differs during loading and unloading (Figure 4). For each pore water pressure, the friction variation is, for the corresponding diameter, within ± 2.5 kPa. The two friction laws obtained were then added to the vertical effective stress calculations. The effective stress corresponds to the net load force applied to the sediment. During loading stages, this force is calculated by subtracting friction force and the vertical upload (force resulting from the area difference between the piston top and bottom, see Figure 3) from the total measured load. During unloading stages, friction is added, as it is always oriented in the direction opposed to piston movement.

The saturation system is composed of two Plexiglas tanks, the same type as the consolidation cell, designed to support 1 MPa of water/gas pressure (Figure 3). Both tanks are connected at the top to a CO_2 bottle equipped with an adjustable pressure gauge that can deliver up to 2.5 MPa of gas pressure (Figure 3). Tanks are half-filled with water, the other half being occupied by gas. Adjustable security valves are connected at the top of the two tanks and allow to expel gas if a pressure threshold is reached (Figure 3). Each tank connects to the top or the bottom of the

consolidation cell by their bottom end. Differential pressures at the top and bottom of the sample can be applied through the two tanks allowing the carbonated water to circulate through the sample.

Pressure gauges control the pore pressure and are limited to 3 MPa with a precision of ± 0.75 kPa. Pressure gauges can be either isolated from the consolidation cell or isolated from the tanks thanks to valves present between the two parts of the system (Figure 3). All the sensors used (load cell, vertical displacement sensor and pressure gauges) are connected to a control panel (Figure 3). The computer monitors, records and controls the different test parameters.

A pressure generator is connected at the bottom end of the consolidation cell for water permeability measurements. The pressure generator creates a pressure gradient while measuring water volume change. Using Darcy's law, it is possible to calculate the hydraulic conductivity of the sediment. A falling head method can also be applied using the differential pressure between the two saturation tanks. Due to the large internal diameter of the saturation tanks (91.9 mm), only hydraulic conductivities obtained from water head variations greater than 10 mm are considered as accurate.

P-wave velocities are measured using GDS bender element system. Due to sample dimensions (diameter: 69.9 mm; initial height around 65 mm), it was necessary to calibrate the signal frequency to avoid a waveguide effect of the Plexiglas cell and lateral rebounds (Chan, 2012). After several tests, a frequency of 100 kHz appeared to record the clearest received signal. To obtain repeatable and comparable measurements, the received signal is picked on the last relative minimum before the first received peak.

The main purpose of this experimental study is to evaluate the impact of gas exsolution and accumulation on the mechanical behavior of the tested sediments (e.g. compressibility, preconsolidation pressure, permeability, P-wave velocity). To do so, several loading/unloading cycles are applied during each test on water-saturated sediments and gassy sediments. Each test can be described with the following basic scheme and phases:

- **Phase 1 - carbonated water**: Water in the two saturation tanks is saturated with CO_2 for at least two days with gas pressure between 300 and 800 kPa. During this first phase, carbonated water is isolated from the consolidation cell (valves closed at the base of the tanks, Figure 3).
- **Phase 2 - saturation using carbonated water**: Remolded sediments are poured into the consolidation cell and connected to the saturation cells. Differential water pressure is applied between the two saturation

tanks, creating a hydraulic gradient and a carbonated water flow through the sediment. The aim is to replace the pure pore water initially present by carbonated water. Circulation is imposed until the carbonated water volume flow reaches the initial total sample volume. During this stage, some gravity settling of sediments can be observed.

- **Phase 3 - consolidation of water-saturated sediments:** The piston is manually moved until contact with sediments is established. The first loading/unloading cycle starts with a loading velocity of 0.12 mm/h and an unloading velocity of 0.5 mm/h. A maximal total load is configured based on the target value of effective stress (σ'_v = 100, 200 or 400 kPa). Another loading/unloading cycle can be applied to record the swelling index of the sediments. During these cycles, P-wave velocity and hydraulic conductivity are regularly measured.
- **Phase 4 - degassing and gas exsolution process**: After unloading, the piston is manually raised to allow gas expansion/exsolution and sediment swelling. Complete or partial depressurization is applied using the two valves connected to the saturation cells (Figure 3). Both valves are opened simultaneously so that the depressurization applies on both side of the sample. The partial gas exsolution is not always visible. Therefore, free gas presence is detected by comparing P-wave velocity before and after depressurization. To ensure full degassing, this phase is maintained for around 15 hours.

Phase 5 - consolidation of gassy sediments: After degassing, contact between the piston and the sample is made manually and generally, a swelling of the sample is noted. The change in the sample height is used to calculate S_g. Another loading/unloading cycle is then applied to the gassy sediments with a σ'_v values exceeding the one applied at phase 4. As loading increases, gas saturation is expected to decrease. During this phase, P-wave velocity and permeability are measured to determine the influence of gas saturation on both parameters.

In the case of partial degassing, the two last phases can be repeated to obtain different gas saturations during the same test. Void ratio, *e*, and gas volume V_{gas} are calculated at each time step using the initial void ratio value (e_0) and the change in sample height. Gas saturation S_g is calculated from pore water volume V_w before degassing and the measured V_{gas}:

$$S_g = \frac{V_{gas}}{V_{gas}+V_w} \quad (1)$$

2.3. Testing program

In the scope of this study, eleven tests were performed, one being a normal consolidation test (no gas and under atmospheric pressure) which is the reference test for compressibility (Table 3). The good agreement between a loading/unloading curve obtained during an oedometer test (ASTM D-2435, ASTM International, 1996) and the present reference test has allowed to validate the used loading velocity. During the ten other tests, fifteen degassing were triggered under different conditions (e.g. preconsolidation pressure, initial gas pressure, u_i, magnitude of depressurization, Δu; Table 3). Sediment mechanical compressibility as well as P-wave velocity and hydraulic conductivity were measured before and after each degassing stage. This study contains 270 P-wave measurements and 26 hydraulic conductivity measurements (Table 3). Details of the testing program are provided in Table 3:

Test number	Cycle (load/unload)	σ'_{vmax} (kPa)	u_i (kPa)	Δu (kPa)	Number of measured V_P	number of measured K	Comments
2	1	100	350	0	13	0	
	2	1000	350	-350	9	0	
	3	1000	350	-350	3	0	
3	1	400	800	0	13	0	
	2	1000	800	-800	6	0	
4	1	200	500	0	19	5	
	2	1000	500	-500	10	0	
	3	1200	0	0	10	0	
5	1	100	800	0	13	2	
	2	1000	800	-800	19	0	
6	1	100	500	0	9	1	
	2	400	500	0	16	1	
	3	1000	500	-500	18	3	
7	1	100	800	0	9	3	
	2	400	800	0	7	0	
	3	1000	800	-400	10	0	
8	1	100	800	0	4	1	
	2	400	800	0	3	0	
	3	1000	800	-300	8	0	
	4	1200	500	-500	3	3	
9	1	400	800	0	7	1	

	2	1000	800	-100	2	0	
	3	1200	700	-250	7	0	
	4	1200	450	-450	4	1	Degassing under σ'_v = 100 kPa
10	1	1200	0	0	9	3	drained consolidation test (reference)
11	1	400	800	0	8	1	
	2	800	800	-200	12	0	
	3	1100	600	-200	11	0	
	4	1400	400	-400	8	1	

Table 3: Testing program with details on the number of loading/unloading cycles per test, the applied maximal effective stress at each stage, the initial gas pressure, the magnitude of depressurization for each exsolution.

3. Results

In the following, we have provided the details of three tests only as, of the eleven tests, test#5, test#8 and test#11 show the main behavioral features observed. The pictures of the sample shown in the results were shot during the tests through the Plexiglas cell.

During test#8, 4 load/unload cycles were applied on the remolded sediment sample (Figure 5a). The first two cycles were completed on the water-saturated sample under constant carbonated water pressure (u_i) of 800 kPa. They showed a normal loading-unloading compressibility curve (Figure 5a). However, the beginning of loading 1 (σ'_v lower than 20 kPa) differs from the reference test. The difference between the two stages is related to the applied carbonated water pressure. A reference test was applied under atmospheric pressure where normal sediment settling took place. For the other ten tests, initial loading (cycle 1) took place under a carbonated water pressure gradient. This affected the normal settling velocity and accelerated sedimentation. After the first unloading in cycle 1, the loading in cycle 2 followed the swelling trend of the sediment until reaching preconsolidation pressure (σ'_{p0} = 100 kPa, σ'_{p0} will be used in the rest of paper to refer to the preconsolidation pressure that the sediment underwent over the last loading phase). From this stage, the sample recovers a normal consolidation trend following the virgin consolidation curve to a vertical effective stress of 400 kPa. The C_c and C_s values are comparable to those obtained from oedometer tests (Figure 2 and Table 2).

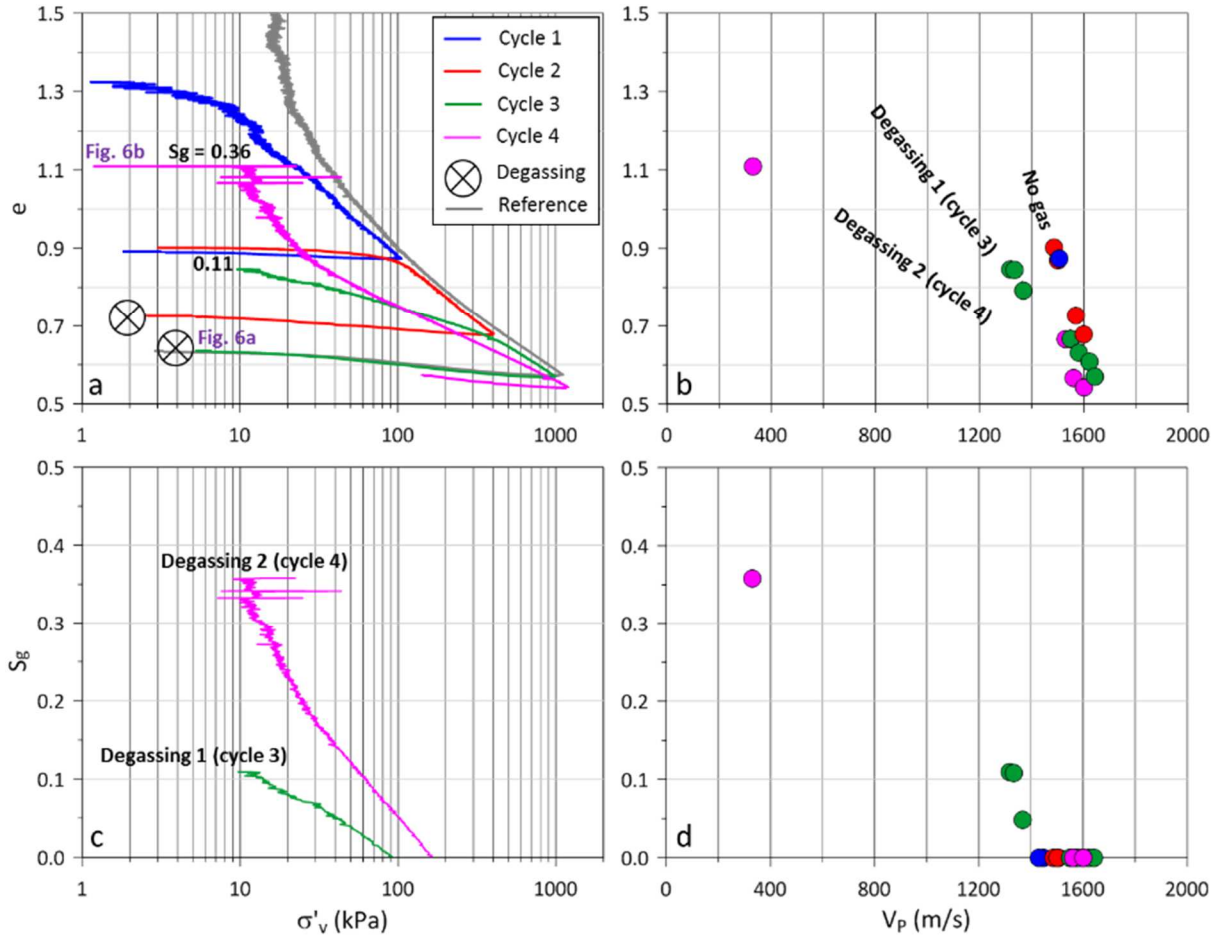

Figure 5: Results for test#8 with 4 load/unload cycles. Each color represents a load/unload cycle. a: void ratio (e) versus vertical effective stress (σ'_v) b: void ratio-versus P wave velocity (V_p); c: degree of gas saturation (S_g) versus σ'_v and d: S_g versus V_p. The grey line in (a) represents the reference consolidation test.

After unloading 2, partial depressurization (Δu) of -300 kPa was applied. No fractures or discontinuities were noticed during this phase. However, the sample swelled by 1.5 mm, corresponding to S_g of 11%. The mechanical behavior after this first degassing stage changed drastically. The sample did not display an elastic trend during reloading showing a compressibility characterized by a slope varying between the swelling index and the compression index (Figure 5a). This intermediate compressibility lasted until reaching an effective stress of 400 kPa corresponding to σ'_{p0}, well after gas saturation reached zero (Figure 5a,c). Then, the compressibility followed the normal compaction trend. P-wave velocities show a constant trend for cycles 1 and 2 (blue and red dots in Figure 5b,d) while the presence of free gas in cycle 3 causes an important decrease in P-wave velocities (green dots in Figure 5b,d). During the loading in cycle 3, S_g decreases and the P-wave velocity increases and reaches normal values only when sediment behaves as a normally consolidated material.

The intermediate compressibility slope (cycle 3 between 20 kPa and 400 kPa in Figure 5a) was calculated and is named C_{Cgas} in all the following tests carried out in this study. For test#8, C_{Cgas} is equal to 0.09. The preconsolidation

pressure was also calculated using the normal elastic curve and the virgin compression curve. The intersection between the two curves gives a preconsolidation pressure that we called σ'_{p2} equal to 130 kPa which is significantly less than the applied 400 kPa in cycle 2 (Figure 5a).

Cycle 4 began with complete depressurization (Δu = -500 kPa) which immediately affected the structure of the sample (Figure 6). Fractures formed during the first minutes following depressurization, ultimately showing a complete remolding of the upper part of the sample (Figure 6). Fractures are horizontally oriented in accordance with the maximum principal stress orientation. This degassing provoked a swelling of 6 mm of the sample partly adapted by the cm-long and mm-thick horizontal fractures (Figure 6). S_g at this stage was found equal to 36% (Figure 5a,c).

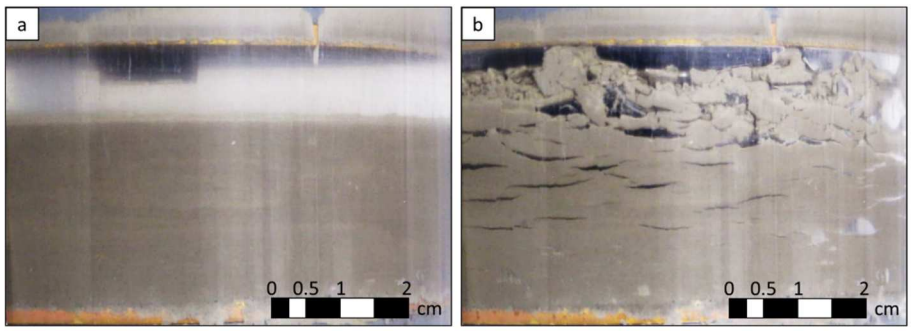

Figure 6: Pictures of the sample during test 8. a: before the second depressurization (cycle 4, Figure 5a) showing the sediment aspect before gas exsolution. b: after the second depressurization (Figure 5a). The sample swelled by 6 mm under the effect of gas exsolution, swelling partly due to the numerous cm-long and mm-thick fractures.

Nageswaran (1983) gives an upper limit for gassy sediments in terms of degree of gas saturation. In this definition, sediments having S_{gmax} higher than 15% should not be regarded as gassy sediments but as unsaturated soil. However, the gaseous phase is not homogeneously distributed and is not continuous as gas invades the sample through fracture generation (Jain & Juanes, 2009). Moreover, once fracture opens, gas exsolution and bubble growth occur predominantly at fracture sites that act as preferential nucleation and bubble growth sites (Jang & Santamarina, 2014; Katsman, 2015). Given the short duration of exsolution (12 hours on average), free gas does not have time to diffuse through the complete sample. Experiments by Cuss *et al.*, (2014) demonstrated that months are needed to saturate a low-porosity sample. Therefore, free gas mainly concentrates in fracture spaces and is not present as separated spherical bubbles as in the Nageswaran (1983) definition.

The loading of cycle 4 can be divided into two stages. The first stage corresponds to the part having a compressibility slope larger than the virgin compression line. This stage corresponds to the fracture closing. Once all the fractures closed, an intermediate compressibility state, similar to that described for cycle 3, is observed. The normal compression trend began at around 900 kPa but is not well expressed since the test was stopped at σ'_v around

297 1000 kPa. S_g reached zero around 180 kPa during the intermediate stage (Figure 5a,c). Again, a drop in P-wave
298 velocities highlights the presence of free gas after gas exsolution (Figure 5b,d). This decrease is greater than during
299 cycle 3 due to greater gas saturation. P-wave velocities shift from the water-saturated values even after S_g reaches
300 zero.

301 The slopes of the two compressibility states during reloading in cycle 4 were also measured. C_{Cgas} equals 0.17.
302 The slope for the state corresponding to fracture closing is named C_{Cfrac} in the following analyses. For cycle 4, C_{Cfrac}
303 reaches 0.7. In this cycle, two preconsolidation pressures can be calculated: σ'_{p2} using the method already described
304 after fracture closing and σ'_{p1} which is calculated using the intersection of the two slopes C_{Cgas} and C_{Cfrac}. σ'_{p1} was found
305 equal to 25 kPa while σ'_{p2} was not calculated because, as mentioned above, the normal compression trend is not well
306 expressed in cycle 4.

307 P-wave velocities display different evolutions with void ratio depending on the cycle (Figure 5b). Cycles 1
308 and 2, where the measurements were made on water-saturated sample, show the same trend while the two other
309 cycles indicate specific trends. P-wave velocities decrease with the presence of free gas (Helgerud, *et al.*, 1999; Sultan,
310 *et al.*, 2012). The impact of free gas on acoustic velocities is well illustrated with test#8 as P-wave velocity trend with
311 void ratio have gentler slope with increasing initial gas saturation (Figure 5b). Decreased values of P-wave velocities
312 were measured even after free gas dissipation ($S_g = 0$), and normal values were reached once sediments followed the
313 normal compression trend (Figure 5a,b,c).

314 During test#11, only one water-saturated cycle was completed, revealing that the sediments have a normal
315 loading/unloading compressibility curve (Figure 7a). Indeed, the virgin compaction curve and the swelling trend of
316 test#11 perfectly fits with the drained consolidation test used as reference (Figure 7a).

317 After unloading 1, partial depressurization (Δu) of -200 kPa is applied. Small and thin fractures appeared along
318 a pre-existing weak zone that expended during gas exsolution (light color strip Figure 8a,b). At the beginning of the
319 loading stage of cycle 2, a swelling of 5 mm was recorded (visible on Figure 8a,b), corresponding to a S_g of 24%
320 (Figure 7a). The compressibility of the gassy sediments during loading 2 is characterized by a slope comprised between
321 C_c and C_s. Here again, it shows an intermediate compressibility before reaching the virgin compression curve once the
322 σ'_{p0} (400 kPa) was exceeded (Figure 7a). S_g reached zero before 200 kPa, therefore, the intermediate compressibility
323 lasted longer than the presence of free gas in the sediments (Figure 7a,c). P-wave velocities decrease after degassing,

compared to the trend obtained on the water-saturated sample during cycle 1 (Figure 7b). Even after the moment S_g reaches zero, P-wave velocities are attenuated, showing that gas exsolution affects them even after free gas entirely dissipated from the sample (Figure 7b,c). Finally, cycle 2 loading reached 800 kPa before unloading the sample once again.

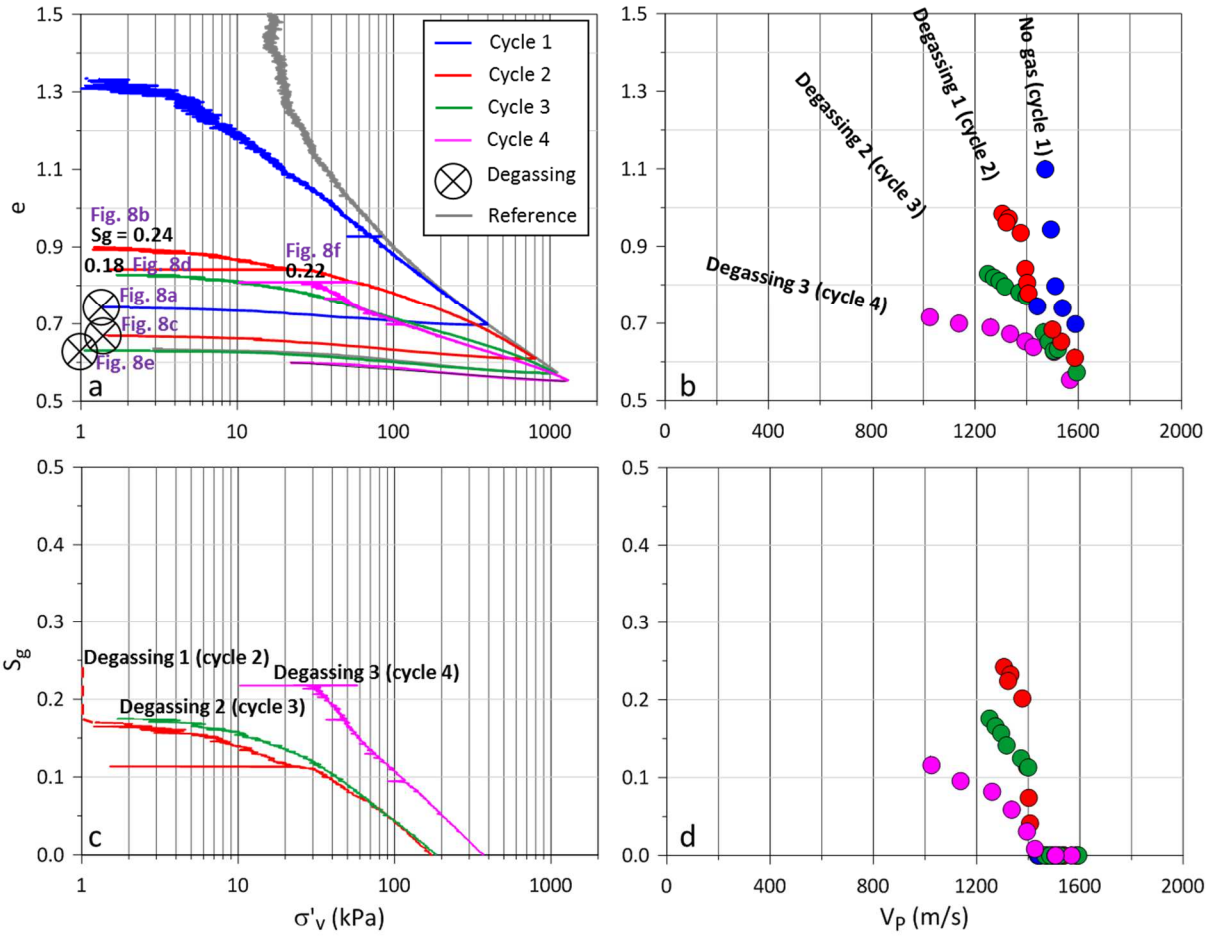

Figure 7: Results for test#11 with 4 load/unload cycles. Each color represents one load/unload cycle. a: void ratio (e) versus vertical effective stress (σ'_v) b: void ratio-versus P wave velocity (V_p); c: degree of gas saturation (S_g) versus σ'_v and d: S_g versus V_p. The grey line in (a) represents the reference consolidation test.

The intermediate compressibility slope C_{Cgas} equals 0.12. Using the swelling and virgin compaction curves, σ'_{p2} was found equal to 100 kPa (cycle 1 reached a σ'_{p0} = 400 kPa).

Cycle 3 started after another partial depressurization of -200 kPa was applied. Rare and localized very thin fractures formed at the base of the sample (Figure 8c,d). No trace of the former weak strip was noticed at this stage. Additionally, 2.7 mm of swelling shows that free gas exsolved in the sample, resulting in a S_g of 18%. An intermediate compressibility is observed until the end of the loading phase. The normal compression trend began at around 900 kPa but is not well expressed since the test was stopped at σ'_v around 1100 kPa. The gas saturation reached zero at only 200 kPa, thus most of the intermediate compressibility was measured on water-saturated sediments (Figure 7a,c). P-

wave velocities are reduced compared to the water-saturated sediment (Figure 7b,d). The depressurization of cycle 3 generated a smaller volume of free gas compared to cycle 2. Nevertheless, P-wave velocities measured during cycle 3 also decreased compared to those of cycle 2 (Figure 7b,d), showing that even after a complete cycle, sediments did not entirely recover their normal acoustic properties.

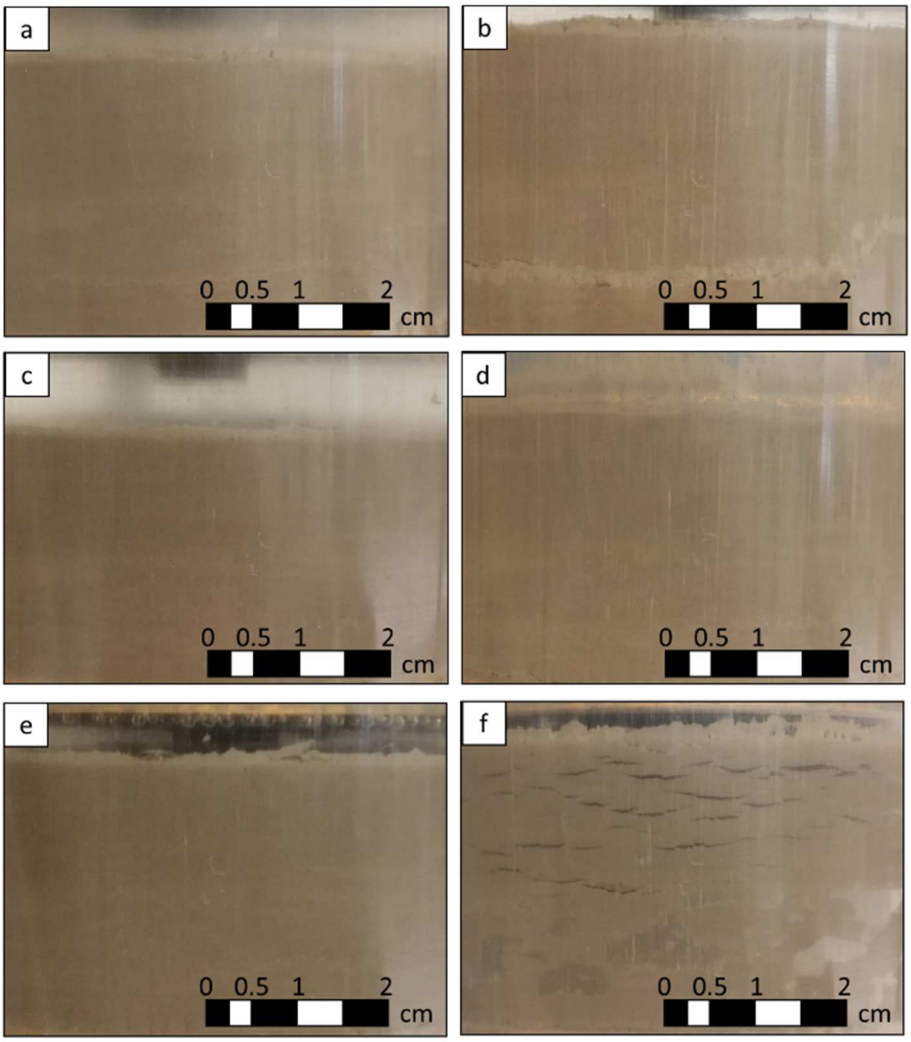

Figure 8: Pictures of the sample during test 11. a: before the second depressurization (cycle 3, Figure 7a) showing the sediment aspect before gas exsolution. b: after the second depressurization (Figure 7a). The sample swelled by 5 mm under the effect of gas exsolution and small and rare fractures appeared along a pre-existing weak zone (lighter color). c: before the second depressurization (cycle 3, Figure 7a) showing the sediment aspect before gas exsolution. d: after the second depressurization (Figure 7a). The sample swelled by 2.5 mm under the effect of gas exsolution with rare and very thin fractures at the base of the sample. e: before the third depressurization (cycle 4, Figure 7a) showing the sediment aspect before gas exsolution. f: after the third depressurization (Figure 7a). The sample swelled by 3.5 mm under the effect of gas exsolution, swelling partly due to the numerous cm-long and mm-thick fractures.

The intermediate compaction slope measurement resulted in a C_{Cgas} of 0.12 and the σ'_{p2} of 180 kPa when σ'_{p0} was 900 kPa (cycle 2).

The final cycle started with complete depressurization (Δu = -400 kPa). Figure 8e,f shows that the sample swelled and fractured during exsolution. The fracture network is dense and composed of centimeter-long and millimeter-thick fractures. Fractures get thinner and thinner towards the base of the sample and some gas pockets are

visible. A total swelling of 3.3 mm was recorded, resulting in a S_g of 22%. The loading of cycle 4 is divided into two stages (Figure 7a). The first stage corresponds to the part having the biggest compressibility. This stage corresponds to the fracture closing (Figure 8f). Once all the fractures closed, an intermediate compressibility state is observed. The normal compression trend began at around 1100 kPa but is not well expressed since the test was stopped at σ'_v around 1300 kPa. S_g reached zero around σ'_v of 380 kPa during the intermediate stage (Figure 7a,c). P-wave velocities recorded during the loading following this depressurization display a strong decrease compared to the other cycle, even compared to cycle 2 during which more free gas exsolved (Figure 7b).

The intermediate compressibility slope, C_{Cgas}, was measured at 0.13. σ'_{p2} was measured at 345 kPa when σ'_{p0} reached 1100 kPa (cycle 3).

P-wave velocities have different trends with void ratio depending on the cycle (Figure 7b). Cycle 1, where P-wave velocities were measured on water-saturated sediments, differs from the other cycles. The impact of free gas on acoustic velocities is again displayed in this test as P-wave velocity trend with void ratio have a gentler slope when sediments contain free-gas (Figure 7b). Once S_g equals zero, P-wave velocities are attenuated until reaching the normal compression trend (Figure 7a,b,c). Moreover, the cycle having the biggest gas saturation is not the one displaying the smallest values of V_P. Instead, P-wave velocities decrease after each gas exsolution showing that sediments did not recover their normal acoustic response after free gas dissipated and reloading.

Only two cycles were completed during test#5. The first cycle is not displayed in Figure 9a as the pressure difference between the two ends of the sample was maintained during the whole cycle for carbonated water circulation. Therefore, the calculated σ'_v for this cycle is not representative. However, total depressurization completed on the sample (Δu = -800 kPa), triggered a complete remolding of sediments as shown in Figure 10. The sample fractured completely and so intensely that it resembled slurry. The total swelling recorded was 9.5 mm, corresponding to gas saturation of 38%, which is the maximum value obtained in this study. For this reason, test#5 is regarded as the extreme scenario. Two intermediate compressibilities were measured. The first one corresponds to the fracture closing and has a sub-vertical slope (Figure 9a). The second one has a slope greater than the virgin compaction curve. Finally, from σ'_v = 150 kPa to the end of the loading, sediments follow the normal compression trend (grey line in Figure 9a). The normal compressibility was recovered when S_g was already equal to zero for 50 kPa

(Figure 9a,c). However, normal compression trends on other tests were recovered with a larger delay from free gas dissipation even though they displayed a lower gas saturation.

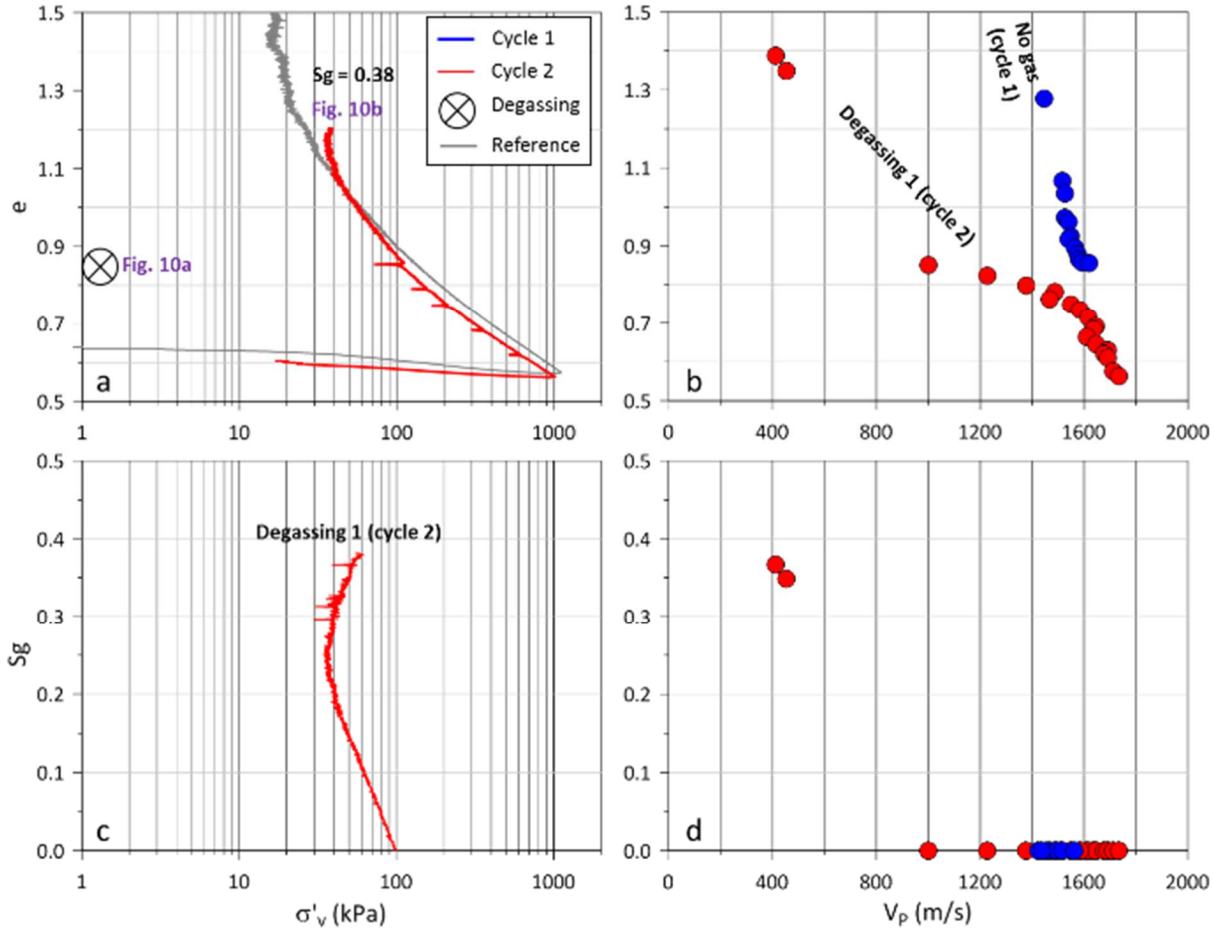

Figure 9: Results for test#5 with 2 load/unload cycles. Each color represents one load/unload cycle. a: void ratio (e) versus vertical effective stress (σ'_v) b: void ratio-versus P wave velocity (V_p); c: degree of gas saturation (S_g) versus σ'_v and d: S_g versus V_p. The grey line in (a) represents the reference consolidation test.

P-wave velocities were recorded throughout the two cycles. Figure 9c,d clearly shows the difference in velocity magnitudes before and after exsolution. P-wave velocities recorded after exsolution decreased by more than 50% for high void ratios (e > 1). After gas dissipation (σ'_v > 100 kPa, Figure 9c), P-wave velocity for cycle 2 quickly increases with decreasing void ratio and recovers a trend parallel to the water-saturated reference when the minimum void ratio for cycle 1 is exceeded (Figure 9b). Therefore, gas exsolution seems to disturb P-wave velocities even after all the free gas has dissipated.

The slopes for the two intermediate compressibilities were measured. The closing of fractures corresponds to a slope C_{Cfrac} of 1.6. The intermediate compressibility slope, C_{Cgas}, was measured at 0.5. Therefore, a σ'_{p1} of 42 kPa was calculated, the initial preconsolidation pressure, σ'_{p0}, being around 60 kPa. σ'_{p2} was not calculated as the classical method for its determination is not applicable in this case. However, due to the slurry aspect of the sample after gas

exsolution (which led to the maximum measured S_g of this study) and based on how the compaction curve fits the reference, this test is considered as representative of a critical remolded state where the sediment has entirely lost its preconsolidation pressure. We consider, for this test, $\sigma'_{p2} = 0$.

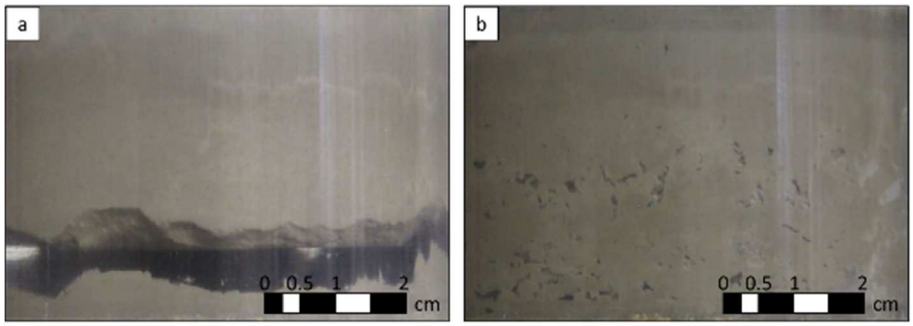

Figure 10: Pictures of the sample during test 5. a: before complete depressurization (Figure 9a) showing the sediment aspect before gas exsolution. b: after complete depressurization (Figure 9a). The sample swelled by 9.5 mm under the effect of gas exsolution. Numerous fractures generated and sediments took a slurry aspect.

4. Synthesis of experimental results

4.1. Fractures, sediment damage and remolding

On the eleven conducted tests, fifteen exsolution events triggered under different conditions (e.g. different σ'_{p0}, different initial degree of gas saturation corresponding to different gas pressure u_g, and different decompression Δu) created diverse fracture distributions, with varying size, shapes and numbers. The observations made on each experiment along with pre-existing conditions are summarized in Table 4.

We propose an empirical classification of fractures, based on the sample visible surface after exsolution. Based on the observations in Table 4, fractures generated by gas exsolution are classified in three different length categories:

1- Fractures longer than 1 cm

2- Fractures between 1 cm and 0.5 cm long

3- Fractures shorter than 0.5 cm.

Conversely, fracturing intensity is arbitrarily grouped in three sets defined as:

1- More than 10 visible fractures

2- Less than 10 fractures

3- No visible fractures.

This classification is empirical and the number of fractures is underestimated as only the sample surface is visible. Nevertheless, as the same classification was applied to all fracture networks, comparison between tests is considered as representative of the actual fracturing intensity.

Test	σ'_{p0} (kPa)	u_g (kPa)	Δu (kPa)	S_{gmax} (%)	fracture type	Photo	Interpretation	Fracture length	Fracture intensity
2	118	350	-350	10	cm-scale connected horizontal fractures. Not numerous. Mainly at the top of the sample.		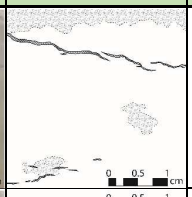	1	2
2	970	350	-350	5	cm-scale and very thin rare fractures.	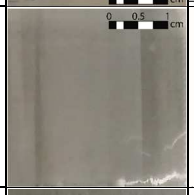	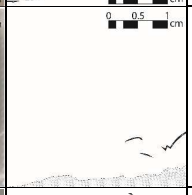	2	2
3	446	800	-800	32	mm-scale horizontal fractures. Numerous. Homogeneously distributed.		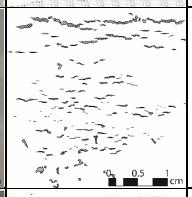	2	1
4	195	500	-500	17	mm-scale horizontal fractures. Numerous. Mainly on the top third of the sample.	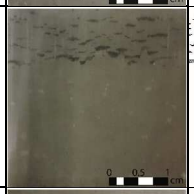	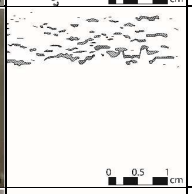	2	1
5	65	800	-800	38	Numerous mm-scale horizontal fractures. Slurry aspect. Completely remolded sediment.	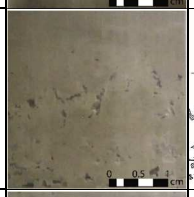	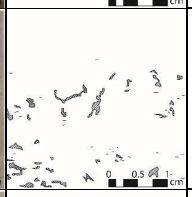	2	1
6	367	500	-500	23	Numerous mm-scale horizontal fractures. Homogeneously distributed.	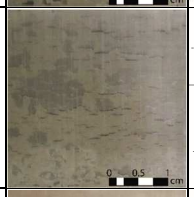	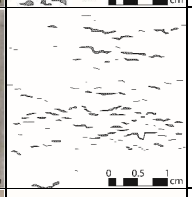	2	1
7	398	800	-400	20	cm-scale horizontal fractures. Not numerous. Sample is cut into two parts.		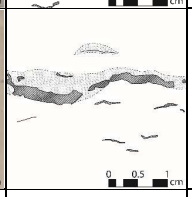	1	2
8	405	800	-300	11	No visible fractures.			3	3

End of Table 4 on the next page

Test	σ'_{p0} (kPa)	u_g (kPa)	Δu (kPa)	S_{gmax}	fracture type	Photo	Interpretation	Fracture length	Fracture number
8	995	500	-500	36	Numerous cm-scale horizontal fractures.	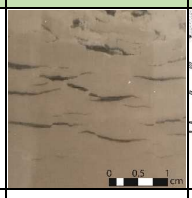	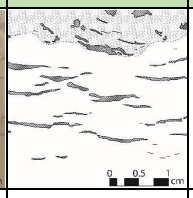	1	1
9	408	800	-100	5	No visible fractures.			3	3
9	895	700	-250	17	No visible fractures.	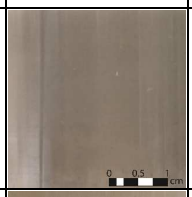		3	3
11	398	800	-200	24	Few mm-scale fractures distributed along a pre-existing light color horizontal layer. Light area thickens during exsolution.		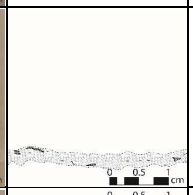	3	2
11	806	600	-200	18	Few mm-scale to cm-scale fractures, mm-thick in the bottom edge of the sample.	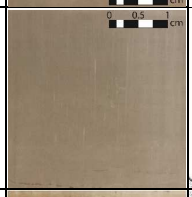	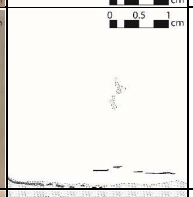	2	2
11	1071	400	-400	22	Numerous cm-scale fractures. Higher fracture number and thicker fractures on the top half of the sample.	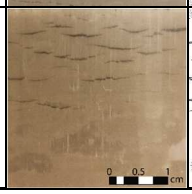	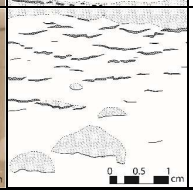	1	1

Table 4: Summary of observations related to fracture networks created during gas exsolution. Each fracture network was classified into three size categories (1: length > 1 cm; 2: 0.5 cm < length < 1 cm; 3: length < 0.5 cm) and three fracture number groups (1: more than 10 fractures; 2: less than 10 fractures; 3: no fractures). Vertical scale is equivalent to the horizontal one on the pictures and their corresponding interpretations. Pictures were taken after each exsolution stage, across the Plexiglas cell.

4.2. Effect of gas saturation on P-wave velocity

The effect of free gas on the acoustic properties of marine sediments has been already widely studied (Helgerud, *et al.*, 1999; Rebata-Landa, *et al.*, 2012; Sultan, *et al.*, 2012). Helgerud *et al.* (1999), based on previous works by Dvorkin *et al.* (1999) on elasticity of marine sediments, proposed an effective medium model to predict P-wave and S-wave velocities in sediments containing free gas and/or gas hydrates based on mineralogy, compressibility and initial void ratio.

We used this model to draw a chart for predicted P-wave velocity variation with void ratio for different values of S_g (black lines in Figure 11a,b). The properties of sediments used in the modeling are summarized in Table 2 (mass% of minerals, C_C). The average number of contacts per grain in a bulk unit (called *n* in the Helgerud *et al.* (1999) model)

was taken as equal to 4. The mineralogy was simplified into three poles (clays, quartz and carbonates) and is indicated in Table 2.

The P-wave velocities obtained from this study were plotted on the theoretical chart (Figure 11a,b). Two variables are considered in Figure 11: the degree of gas saturation (Figure 11a) and the maximum degree of gas saturation for each cycle (Figure 11b). Figure 11 also displays two examples of signals that are considered reliable for the V_P determination: one with a high degree of gas saturation, after gas exsolution (Figure 11c), the other on a water-saturated and undisturbed sample, before gas exsolution (Figure 11d).

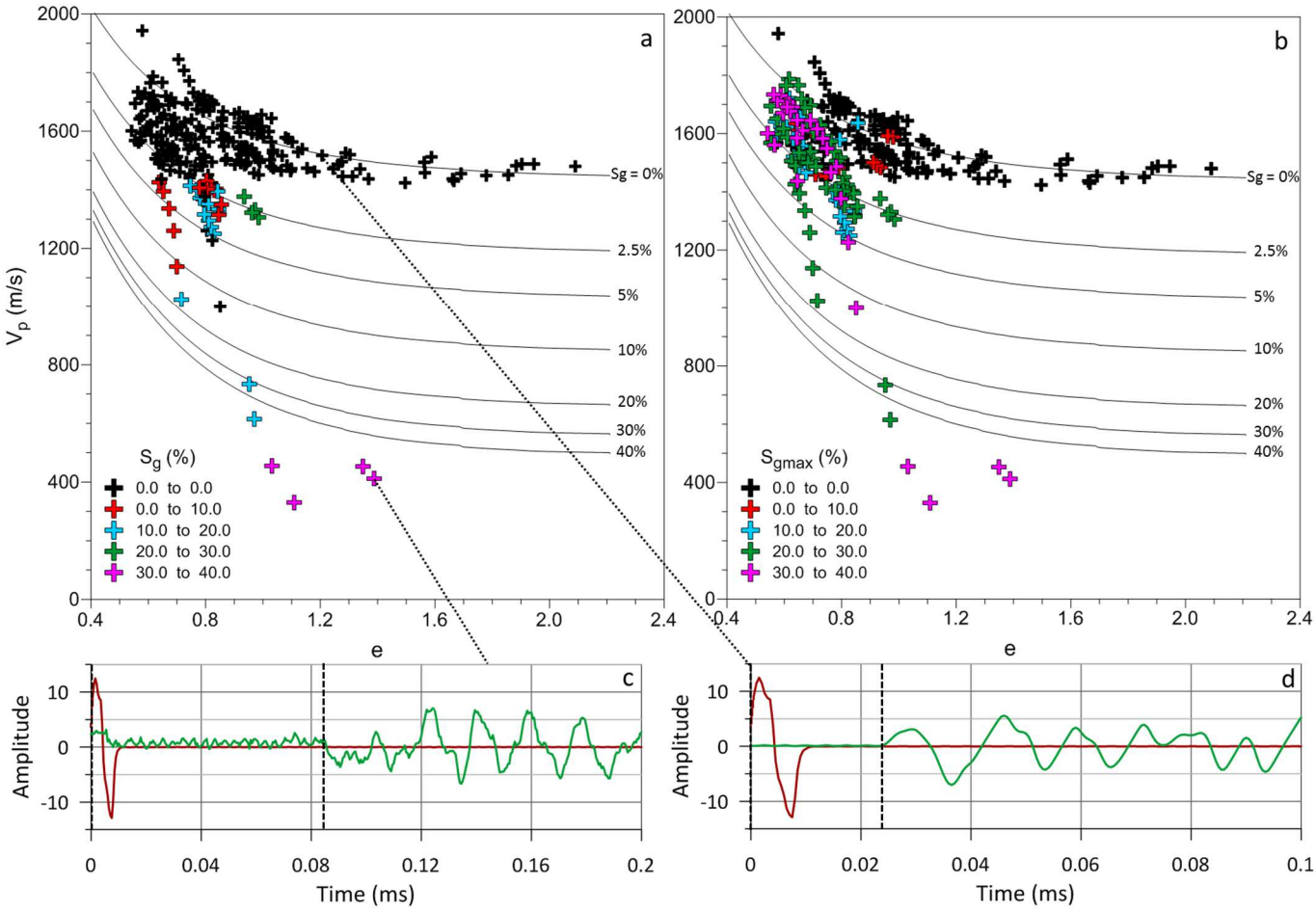

Figure 11: P-wave velocity (V_P) versus void ratio (e). Colors stand for (a) S_g (%) and (b) S_{gmax} (%). Black lines correspond to the evolution of V_P with e for different values of S_g based on the effective medium theory modeling (Helgerud, *et al.*, 1999)*. (c) is the typical signal after gas exsolution, (d) is the typical signal after gas exsolution. Red line corresponds to the source signal, green line is the received signal.*

The first observation is the good agreement between the curve corresponding to S_g = 0% on the chart and the P-wave velocity measurements obtained before exsolution (Figure 11a). Once exsolution occurs, P-wave velocities decrease drastically even for low values of S_{gmax} (red and blue crosses on Figure 11b). For the highest values of S_{gmax}, this decrease reaches 75% of the water-saturated value for a given void ratio. During the loading stage following exsolution, free gas is dissolved or expelled from the sample and S_g decreases. Accordingly, P-wave velocities increase

once again (Figure 11a). Once S_g reaches zero, P-wave velocities remain below the reference values and follow a trend between the curve corresponding to S_g = 0% and S_g = 2.5% (Figure 11a).

4.3. Effect of degree of gas saturation on sediment compressibility

During the tests completed during this study, a clear difference in sediment compressibility was observed when comparing the state before and after gas exsolution. The compressibility after gas exsolution has a slope comprised between C_C and C_S called C_{Cgas}. When fractures were abundant and/or large enough, a first compressibility state was observed with slopes generally larger than C_C and called C_{Cfrac}.

For a comparative analysis, values of C_{Cgas} and C_{Cfrac} obtained from the different tests were plotted against the maximum degree of gas saturation determined during each loading/unloading cycle (S_{gmax}) and were then compared to C_C and C_S of water-saturated sediments (Figure 12). C_{Cgas} are all comprised between the C_C and the C_S of water-saturated sediments.

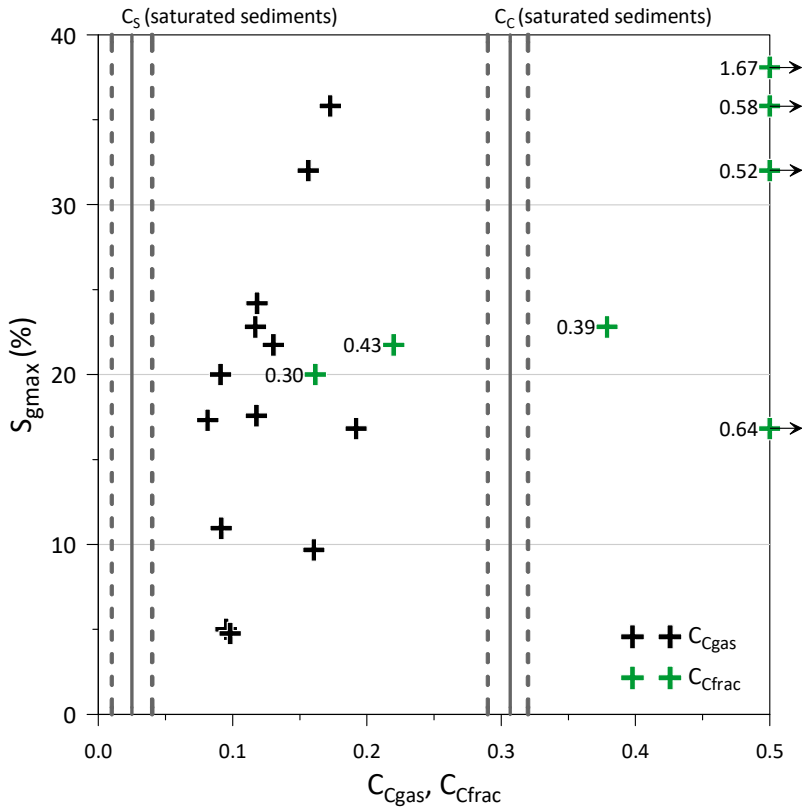

Figure 12: Compressibility versus S_{gmax} (%). Two type of compressibility are displayed. The grey vertical lines stand for the water-saturated sediments C_C and C_S, the dotted lines being the maximal and minimal values obtained during the different tests. Values of C_{Cfrac} are annotated as labels, since values above 0.5 were plotted at 0.5 to condense the graph.

C_{Cfrac} values, except for two cases, are much larger than the C_C of water-saturated sediments. This compressibility slope, observed after fracture initiation, corresponds to fracture closing. C_{Cfrac} obtained from tests 7 and 11 are lower than C_C. Test 7 fracture network is unique as a large fracture split the sample in half (Table 4), and

contact between the two halves occurred when the fracture closed. For test 11, the fracture network is one of the densest, with centimeter-scale fractures. Before reloading (cycle 4), a permeability measurement under an imposed vertical hydraulic gradient partially closed the thinner fractures. This could be an explanation for the lower values of C_{Cfrac} obtained on both tests.

4.4. Hydraulic Conductivity versus degree of gas saturation

Hydraulic conductivity (K) data versus void ratio are shown in Figure 13a. K values obtained on the same sediment using the classical falling head method are plotted for comparison.

K measurements made before exsolution on water-saturated samples fit well with odometer measurements (Figure 13a). After gas exsolution, K increases above the water-saturated sample trend. Thereafter, K decreases rapidly while resuming reloading, and reaches values below the trend of water-saturated samples. This decrease happened during a short time interval compared to the decrease of K during consolidation of the water-saturated sample. However, some of the K values acquired on water-saturated sediments seem to spread relatively to the trend curve in the same way. Nevertheless, Figure 13b clearly shows that K increases with the S_g.

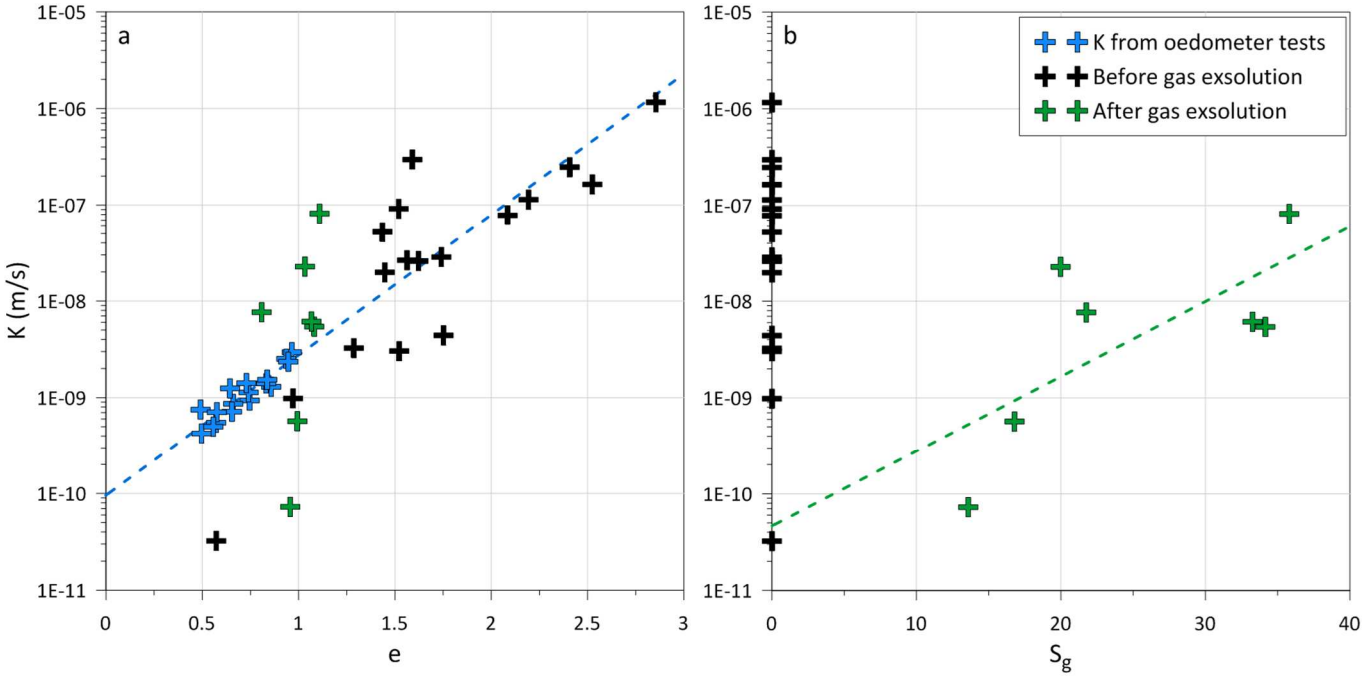

Figure 13: a: hydraulic conductivity, K (m/s) versus void ratio. The blue dashed line is an exponential fit for hydraulic conductivities on water-saturated sediments obtained from oedometers (blue crosses). b: K (m/s) versus S_g (%).

4.5. Preconsolidation pressure evolution with degree of gas saturation

In this paper, two preconsolidation pressures were determined. Before fracture closing, the intersection between the two slopes corresponding to C_{Cfrac} and C_{Cgas} gives the σ'_{p1}. After fracture closing, σ'_{p2} was determined by the intersection of the swelling curve and the virgin compaction curve.

To compare the two parameters over the entire set of test results, we normalized them with respect to σ'_{p0} (Figure 14). The $\sigma'_{p1}/\sigma'_{p0}$ increases generally with increasing S_{gmax} but without a clear tendency (Figure 14a). Moreover, comparing these values to fractures in Table 4 shows that there is no clear relationship between fracture size and number and $\sigma'_{p1}/\sigma'_{p0}$.

Regarding the ratio between σ'_{p2} and σ'_{p0}, results show that it decreases with increasing S_{gmax}, evidencing a preconsolidation pressure degradation with S_{gmax} (Figure 14b). As a comparison, values from the study by Sultan, *et al.* (2012), on gassy sediments from the Gulf of Guinea were also added to Figure 14b. The results show a clear logarithmic trend with a strong determination coefficient of 0.75 and starting with a ratio equal to 1 when S_g is zero. Values from the Gulf of Guinea are not exactly on the proposed trend. They were obtained on sediments having a completely different behavior in a water-saturated state, with a C_C as high as 2 (Colliat, *et al.*, 2011).

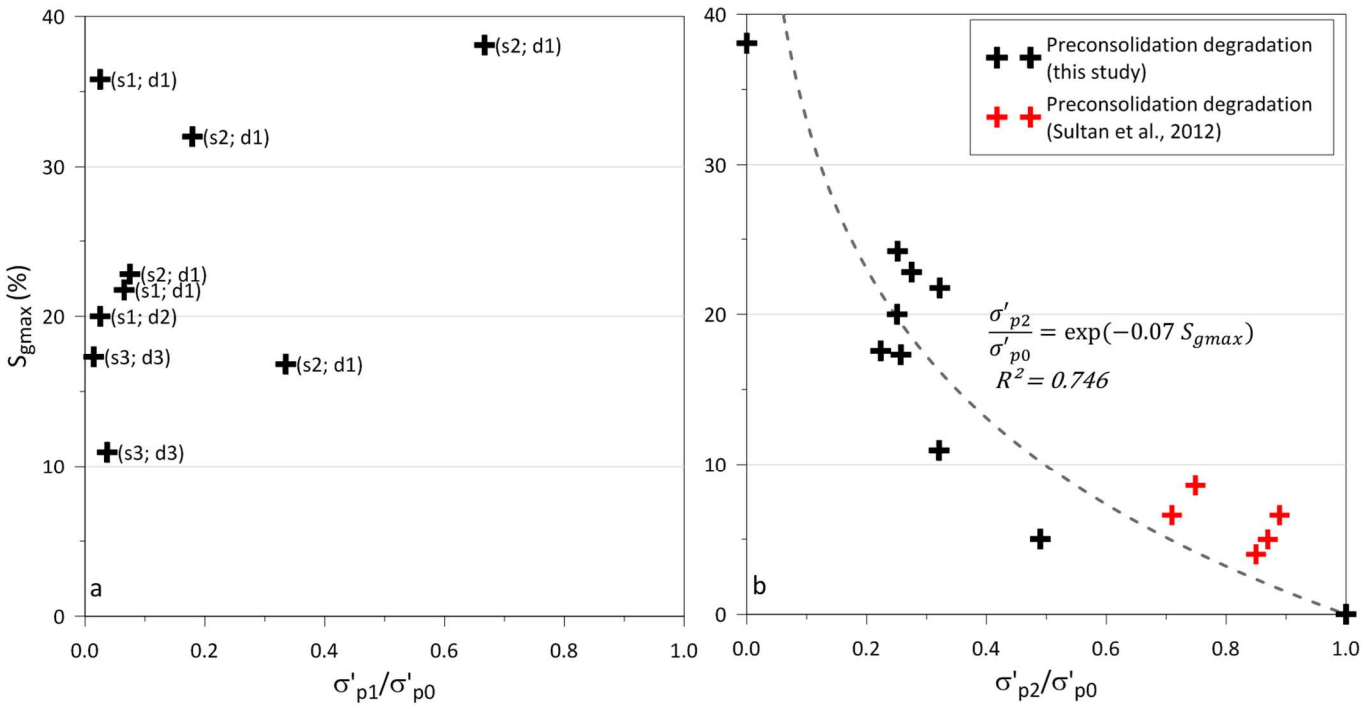

Figure 14: Preconsolidation ratio versus S_{gmax} (%). a: ratio between preconsolidation pressures calculated before fracture closing, σ'_{p1}, and the initial preconsolidation pressure, σ'_{p0}. The labels correspond to the fracture classification given in Table 4. "s" stands for the fracture length, "d" for the fracture number. b: ratio between preconsolidation pressures calculated after fracture closing, σ'_{p2}, and the initial preconsolidation pressure, σ'_{p0}. Values from Sultan, *et al.* (2012) *are also plotted as comparison (red crosses). An exponential fit of the study results shows a strong determination coefficient (R^2).*

5. Discussion

5.1. Fracture size and number: main controlling factors

The classification of fractures depending on their size and number was compared to the other parameters used or obtained during the testing program (e.g. σ'_{p0}, Δu or S_{gmax}; Table 4). The aim is to identify the main parameters controlling fracture size and number.

First, the length of fractures formed during this study range from one mm to few cm. Their observable thicker part corresponds to the center of the crack. Boudreau (2012) shows that growth and rise of gas bubbles in sediments is possible through fracture generation and that bubbles will be disk-shaped (also demonstrated by Katsman (2015)). Shin & Santamarina (2011) as well as Jain & Juanes (2009) show that gas-driven fractures are favored in fine-grained sediments. Therefore, gas exsolution and subsequent bubble generation and growth explains the shape of fractures. The observed cracks are not pre-existing discontinuities.

It clearly appeared during our study that the S_{gmax} controls the fracture number: the larger the volume of free-gas generated, the bigger the number of fractures. However, noticeable exceptions, such as test#11, show that this is not the unique controlling factor for fracture number. A secondary parameter, the magnitude of depressurization (Δu), seems to modulate the fracture number: the higher Δu, the more numerous the fractures. The two parameters are closely related as the S_g, corresponding to a volume of free gas generated during exsolution, is a direct consequence of the magnitude of depressurization.

From visual observations, three main fracture distributions can be discriminated (Table 4): dense and small fractures (tests 3, 4, 5 and 6), dense and large fractures (tests 8 and 11), and rare or inexistent fractures (tests 2, 8, 9, and 11).

The two denser distributions correspond to high S_{gmax} values (more than 20%) reached by complete depressurization. Test#4 is an exception. It presents a very dense fracture network but only at the top of the sample. The sample was clearly not entirely saturated with carbonated water hence explaining fracture distribution. Besides, S_{gmax} is calculated for the complete sample. Thus, applied to the fractured volume, S_{gmax} is much higher than calculated. Smaller S_{gmax} or partial depressurization lead to fracture networks with few or no fractures at all.

Preconsolidation pressure (σ'_{p0}) is the controlling factor of fracture size. Observation of the two groups with dense fracture networks (high S_{gmax}) shows that when σ'_{p0} is small (below 500 kPa) fractures are small. For higher σ'_{p0} (above 500 kPa), these fractures get longer and thicker. Various studies on bubble growth and shape in marine sediments yielded the same results. Boudreau *et al.*, (2005), Barry & Boudreau (2010) and Katsman, (2015) demonstrate that bubble shape and size is mainly controlled by the mechanical properties of sediments. In particular, Katsman (2015) concludes that bubbles generating in weak sediments are small with higher surface-to-volume ratio (thin bubbles) while bubbles forming in stronger sediments tend to be larger and more spherical (larger).

Therefore, the controlling factors for fracture network architectures are S_{gmax} and Δu both controlling the number of fractures while σ'_{p0} controls the size of the fractures.

5.2. Gas exsolution/expansion: a permanent P-wave velocity attenuation?

The presence of free gas has been always an issue when dealing with P-wave velocities (Sills, *et al.*, 1991; Helgerud, *et al.*, 1999; Sultan, *et al.*, 2012). It provokes strong attenuation of the signal, ultimately preventing any signal propagation. Therefore, P-wave velocities are often used as a tool to detect free gas formation (Rebata-Landa, *et al.*, 2012; Sultan, *et al.*, 2012) as well as for estimating a degree of gas saturation (Lee & Collett, 2006; Morgan, *et al.*, 2012). The acoustic response of gassy sediments is theoretically supposed to join the trend of saturated sediments whenever S_g becomes equal to zero.

The present study confirms this attenuating effect of free gas on P-wave velocities (Figure 11). The higher the S_g, the stronger the P-wave velocity attenuation. Besides, as free gas is dissolved and compressed during reloading, P-wave velocities increase once again. It shows the strong correlation between P-wave velocities and the S_g. Nevertheless, during reloading, when S_g reaches zero, P-wave velocities remain attenuated compared to the normal trend for water-saturated sediments (Figure 11a). Therefore, the damage generated by gas exsolution seems to delay the normal acoustic response of the sample.

The presence of fractures is a known factor for attenuating P-wave velocities in the perpendicular direction, independently of its filling material (Anderson, *et al.*, 1974; Kahraman, 2002; Leucci & Giorgi, 2006; Popp & Salzer, 2007). Fracture generation may have triggered local changes in the shear modulus and/or the bulk modulus of the sediment (Huang, *et al.*, 1995). Therefore, even after mechanical reloading and water saturation, long-term impact of fractures on the acoustic response is expected.

559 Moreover, Helgerud's model, predicting P-wave velocities for given S_g's (Helgerud, *et al.*, 1999), does not fit
560 with most of the P-wave velocities recorded after gas exsolution (Figure 11a). P-wave velocities are greatly
561 overestimated (up to 300 m/s) for samples where dense fracture networks appeared during gas exsolution (Table 4)
562 and they are underestimated (less than 100 m/s) for samples presenting rare or no fractures after gas exsolution
563 (Table 4). P-wave velocities measured on samples with a higher degree of gas saturation present a signal that can be
564 misleading. This may lead to errors in measurement that partly explain the differences observed with the model
565 (≈100 m/s). Considering the potential errors in measuring P-wave velocities for gassy samples, the Helgerud model is
566 in adequacy with the measurements made on samples without or with rare fractures. The impact of fractures and
567 discontinuities in the sample over P-wave velocities is responsible for the rest of the discrepancy, as modeled values
568 are calculated for a homogeneous medium.

569 Thus, sediment damage caused by gas exsolution (through fractures, or with no visible markers), seems to
570 have a durable impact on acoustic properties of sediments.

571 ### 5.3. Gas exsolution/expansion effects on sediment compressibility

572 Sultan, *et al.* (2012) have clearly identified the impact of gas exsolution on the compressibility of clayey
573 sediments. Experimental data of Sultan, *et al.* (2012) showed that after gas exsolution, the compressibility of the
574 sediments increased significantly and is between the swelling index and the compression index of the initial intact
575 sediments. This compressibility degradation was interpreted as being the result of sediment damaging during free gas
576 generation. Previous experiments also highlighted a decay of compressibility with the presence of gas bubbles in soft
577 marine clays (Sills, *et al.*, 1991; Nava Castro, *et al.*, 2013; Liu, *et al.*, 2016). They concluded that gas bubbles bear part
578 of the load applied on the sample and that soil compressibility measured on gassy sediment is primarily due to bubble
579 compression and secondarily due to normal sediment compression, implying water expulsion. The presence of free
580 gas in sediments was also proved to be responsible for a delay in consolidation. As gas escapes or dissolves,
581 consolidation happens faster (Sills, *et al.*, 1991; Nava Castro, *et al.*, 2013).

582 This study showed that gas exsolution creates two intermediate compressibilities after fracture generation
583 (C_{Cfrac} and C_{Cgas}) and only one when no fractures appeared (C_{Cgas}) (Figure 5a, Figure 7a and Figure 9a). The formation of
584 fractures strongly impacted the compressibility of sediments. C_{Cfrac} were only measured for dense fracture networks
585 and were generally higher than C_C (Figure 12). Conversely, fracture number affected the compressibility after fracture

586 closure (C_{Cgas}). For equivalent S_{gmax}, higher C_{Cgas} were recorded for higher number of fractures (Table 4 and Figure 12).
587 C_{Cgas} was always comprised between C_C and C_S (Figure 12).

588 Nevertheless, C_{Cgas} were also measured when no fractures were generated in the sediments. This shows that
589 if fractures have an impact on the compressibility of sediments, the main controlling factor is the presence of gas.
590 Indeed, this study shows that when S_{gmax} increases, C_{Cgas} increases (Figure 12). For low S_{gmax}, C_{Cgas} is closer to the
591 swelling index of water-saturated sediments. This correlation was also noted by Hight & Leroueil (2003) during loading
592 of a sample with occluded gas bubbles. Therefore, gas exsolution tends to destroy the elastic behavior of sediments.

593 Test#5 displayed an extreme behavior with a slurry aspect after gas exsolution and a C_{Cgas} higher than C_C. The
594 virgin compaction curve was reached very fast compared to other tests (Figure 9a) showing that, after gas exsolution
595 in test#5, the sediments behaved as the initial remolded sediment.

596 Moreover, compressibility recovers a normal trend once σ'_{p0} is reached, long after S_g reached zero. Hight &
597 Leroueil (2003) demonstrated that once gas bubbles collapsed during reloading of a sample containing occluded gas
598 bubbles, it recovers its normal C_C. The difference in this study is that free gas is concentrated along fracture planes
599 and is not in the form of occluded gas bubbles. Therefore, as for P-wave velocity attenuation, the delay in
600 compressibility recovery may be due to a permanent impact of fractures and damage caused by gas exsolution.

601 ## 5.4. Gas exsolution/expansion effects on sediment permeability

602 Permeability of sediments can be affected by several mechanisms. Normal consolidation of sediments results
603 in a decrease in hydraulic conductivity (Olsen, 1960; Chu, *et al.*, 2002), contrarily to the presence of fractures, which
604 may enhance this permeability depending on the fracture orientation relative to hydraulic gradient (Alfaro & Wong,
605 2001). Besides, free gas in fine-grained sediments were proved to be a factor for permeability reduction (Egermann &
606 Vizika, 2000; Naylor, *et al.*, 2000; Hight & Leroueil, 2003; Jang & Santamarina, 2014). If free gas accumulates in clayey
607 layers, a capillary seal may form (a gas cap), generating an effective permeability even lower than the intrinsic
608 permeability of the clayey layer (Revil, *et al.*, 1998; Cathles, 2001).

609 Gas exsolution triggered the formation of horizontal millimeter to centimeter-scale fractures. Their orientation
610 corresponds to a direction orthogonal to the possible fluid expulsion, which is not favorable to an increase in
611 permeability. However, as observation of the fracture network was only possible at the sample surface, it is possible

that fluid pathways created through connections between fractures, thus explaining the observed increase in permeability right after gas exsolution (Figure 13). These fractures were filled with free gas after gas exsolution, which may rather be a parameter in favor of a decrease in permeability. However, we do observe an increase in sample permeability just after fracture creation showing that gas filling the fractures may be in a continuous phase through an interconnected fracture network (Jang & Santamarina, 2014).

During reloading, the rapid decrease in permeability (Figure 13) is probably related to the closing of fractures, and the consequent reduction of fluid pathways. Consequently to fracture closing, trapping of free gas in reduced areas changes free-gas distribution from a continuous phase to a more discrete distribution, a factor that was proved by Jang & Santamarina (2014) to reduce sample permeability. The creation of potential capillary seals along the former fracture planes could explain the hydraulic conductivity values that are below the normal trend (Cathles, 2001).

Therefore, gas exsolution provokes an increase in permeability through fracture creation, creating preferential pathways. Then, reloading quickly reduces permeability due to fracture closure and capillary sealing as a consequence of free gas being captured in a discrete distribution.

5.5. Gas exsolution/expansion effects on preconsolidation pressure and the consequence in terms of shear strength

Besides the fracture formation that has already been discussed, gas exsolution has an impact on the preconsolidation pressure of sediments, showing the degree of sediment damage caused.

Before fracture closing, the degradation of sediment preconsolidation pressure is significant but seems to decrease with S_{gmax} (Figure 14a). However, no clear trend appears. Except for one value, corresponding to test#5, all the ratios are below 0.35. It tends to indicate that at 35% of the σ'_{p0} fractures are closed as σ'_{p1} indicates a degradation connected to fracture closing. The sample of test#5 was completely fractured during gas exsolution explaining the high value for the $\sigma'_{p1}/\sigma'_{p0}$ ratio: fractures took more time to close.

σ'_{p2} was measured after fracture closing, therefore it evaluates the part of sediment damage that is visually imperceptible. The ratio between σ'_{p2} and σ'_{p0} correlates with S_{gmax} through a logarithmic law (Figure 14b): the bigger S_{gmax}, the more the sediment was remolded, recording a decrease in preconsolidation pressure. This type of relation was already noted on sediments from the Gulf of Guinea (Sultan, *et al.*, 2012) but at lower S_{gmax} (below 10%). Besides,

several other studies demonstrated this decrease in presconsolidation pressure with an increasing degree of gas saturation (Lunne, *et al.*, 2001; Hight, *et al.*, 2002). For Hight & Leroueil (2003), it is mainly the result of damage due to bubble-growth in the sediments, the degree of damage being related to the initial level of structure. The initial level of structure may be the explanation for the differences observed between the measurements made during this study and the results obtained by Sultan, *et al.* (2012) on a different sediment.

This study showed, for different sediments and at a higher S_{gmax} that a complete loss of preconsolidation pressure is feasible. For 38% of S_{gmax}, preconsolidation pressure was completely lost, showing that sediments were entirely remolded by gas exsolution. The corresponding sample (test#5) had a slurry aspect right after gas exsolution and displays extreme behavior in terms of compressibility and sediment damage.

Therefore, the experimental results confirm that gas exsolution causes sediment damage and remolding. For strong gas exsolution, leading to high S_{gmax}, sediments can even reach a state where they entirely lose their preconsolidation pressure.

Wheeler (1988) showed that methane bubbles might decrease or increase the undrained shear strength of reconstituted silty-clay samples. This was shown to depend on the level of total and effective stress. In the Wheeler (1988) experiments, gas bubbles were formed artificially by using the zeolite molecular sieve technique. Gas naturally formed in sediments or was generated by circulation of carbonated water. Subsequent decompression was shown to negatively affect the undrained shear strength. Lunne, *et al.* (2001), Hight, *et al.* (2002) and Sultan, *et al.* (2012) all point out that the degree of gas saturation significantly reduces preconsolidation pressure and shear strength.

Sultan & Garziglia (2014) proposed a constitutive model to simulate the mechanical behavior of gassy sediments where preconsolidation pressure is the main parameter controlling yield surface and therefore shear strength of the sediment. By introducing to a conventional Cam-Clay type model the “preconsolidation pressure - degree of gas saturation” logarithmic relationship equivalent to the one shown in Figure 14b, they were able to reproduce the observed data published by Lunne, *et al.* (2001), Hight, *et al.* (2002) and Sultan, *et al.* (2012). Data shown in Figure 14b highlight the important consequence of gas formation on the shear strength of the sediment from the AMV where the damage due to bubble growth may strongly decrease its shear strength. A S_{gmax} of 38 % seems to be

664 the upper limit for complete destruction of the structure and therefore the shear strength of AMV sediments and
665 favoring mud generation.

666 6. Conclusions

667 This study investigates the impact of gas exsolution on the mechanical behavior of mud samples recovered on
668 mudflows expelled from the Absheron Mud Volcano. The goal was to understand the factors that control fine-grained
669 sediment damaging, and to quantify and determine the criteria by which we may determine that sediments are
670 completely remolded, and considered as changed into mud. Eleven consolidation tests using a novel experimental
671 apparatus allowed to generate free gas under different consolidation conditions. Results show that:

672 1- Fracture number is controlled by the degree of gas saturation, while preconsolidation pressure mainly
673 controls fracture length.
674 2- Gas exsolution provokes sediment damage (through fracture emplacement and loss of preconsolidation
675 pressure) and it increases with the degree of gas saturation while the elastic modulus of sediments is partly
676 lost. Shear strength is also expected to decrease as a consequence of sediment damage.
677 3- Acoustic response remains degraded long after free gas has entirely dissipated from the sample.
678 Compressibility is also durably modified, reaching normal trends only when initial preconsolidation is
679 exceeded. Permeability first increases through fracture creation, but quickly deteriorates due to the
680 presence of gas leading to capillary sealing during reloading. Therefore, sediments do not recover entirely
681 from gas exsolution damage during reloading.
682 4- During testing, critical behavior was observed for a degree of gas saturation of 38%. Gas exsolution
683 triggered complete remolding of sediments (entire loss of preconsolidation pressure and therefore its
684 shear strength) that took a slurry aspect. The same test displayed the highest compressibility at the
685 beginning of reloading. Its compressibility trend was close to the initial compaction behavior whilst
686 sediments had not yet compacted. Therefore, gas exsolution alone was able to generate mud from
687 compacted fine-grained sediments.

688 Our experimental results showed that gassy fine-grained sediments with discontinuous gas phase may take
689 place for Sg greater than 15 %. We show that such an experimental study can help determine the criteria for mud

690 generation under laboratory conditions and on a particular sediment sample: mud expelled from the Absheron Mud
691 Volcano. These criteria can be implemented into numerical models, integrating mechanical behaviors under the
692 geological conditions observed and determined in the field. Ultimately, this experimental study offers a unique
693 opportunity to quantify the volume of gas required to generate the volume of mud at depth that was extruded to form
694 the studied Absheron Mud Volcano.

695 Acknowledgments

696 Data describing the natural mud properties are available at the following link:
697 https://figshare.com/articles/Absheron_mud_analysis/7448153. This study was conducted in the scope of the PhD of
698 Arthur Blouin under the joint direction of the Pau University (E2S-UPPA), Ifremer and Total S.A. The authors would like
699 to thank Claire Fialips for the mud mineralogy analysis, Mickaël Rovere for his help during compressibility/permeability
700 analyses, as well as Mickaël Roudaut and Ronan Apprioual for the experimental set-up conception/assembly and their
701 technical support. Constructive comments by the associate editor and two anonymous reviewers helped to improve
702 the paper.

703 References

704 Alfaro, M. C. and Wong, R. C. K. (2001) 'Laboratory studies on fracturing of low-permeability soils', *Canadian*
705 *Geotechnical Journal*, 38(2), pp. 303–315. doi: 10.1139/cgj-38-2-303.

706 Anderson, D. L., Minster, B. and Cole, D. (1974) 'The effect of oriented cracks on seismic velocities', *Journal of*
707 *Geophysical Research*, 79(26), pp. 4011–4015.

708 ASTM International (1996) 'D 2435 – 96 - Standard test method for one-dimensional consolidation properties
709 of soils', *American Society for Testing and Materials*. West Conshohocken, 04.08, pp. 196–205. doi: 10.1520/D2435-
710 96.

711 Barry, M. and Boudreau, B. P. (2010) 'First-order description of the mechanical fracture behavior of fine-
712 grained surficial marine sediments during gas bubble growth', *Journal of Geophysical Research: Atmospheres*, 115, pp.
713 1–10. doi: 10.1029/2010JF001833.

714 Blouin, A. *et al.* (2019) 'Evolution model for the Absheron mud volcano : from in - situ observations to

715 numerical modeling', *Journal of Geophysical Research: Earth Surface*, 124(3), pp. 766–794. doi:
716 10.1029/2018JF004872.

717 Boggess, R. and Robertson, P. K. (2011) 'CPT for Soft Sediments and Deepwater Investigations', *Offshore*
718 *Technology Conference*, 21244(May), pp. 2–5.

719 Boudreau, B. P. *et al.* (2005) 'Bubble growth and rise in soft sediments', *Geology*, 33(6), pp. 517–520. doi:
720 10.1130/G21259.1.

721 Boudreau, B. P. (2012) 'The physics of bubbles in surficial , soft , cohesive sediments', *Marine and Petroleum*
722 *Geology*. Elsevier Ltd, 38(1), pp. 1–18. doi: 10.1016/j.marpetgeo.2012.07.002.

723 Capaccioni, B. *et al.* (2017) 'Sand volcano generated by a violent degassing from methane-saturated aquifers:
724 The case study of Medolla (Modena, Italy)', *Engineering Geology*. Elsevier B.V., 221(May 2012), pp. 91–103. doi:
725 10.1016/j.enggeo.2017.02.027.

726 Cathles, L. M. (2001) 'Capillary seals as a cause of pressure compartmentation in sedimentary basins', in
727 *Petroleum Systems of Deep-Water Basins: Global and Gulf of Mexico Experience. 21st Annual Bob F. Perkins Research*
728 *Conference*. Gulf Coast Section of the Society of Economic Paleontologists and Mineralogists, pp. 561–572. doi:
729 10.5724/gcs.01.21.0549.

730 Chan, C. M. (2012) 'On the intepretation of shear wave velocity from bender element tests', *Acta Technica*
731 *Corviniensis - Bulletin of Engineering*, 5(1), pp. 29–34. Available at: http://acta.fih.upt.ro/pdf/2012-1/ACTA-2012-1-
732 03.pdf.

733 Chu, J. *et al.* (2002) 'Consolidation and Permeability Properties of Singapore Marine Clay', (September), pp.
734 724–732.

735 Colliat, J.-L. *et al.* (2011) 'Gulf of Guinea deepwater sediments: Geotechnical properties, design issues and
736 installation experiences', in White, D. and Gourvenec, S. (eds) *Frontiers in Offshore Geotechnics II*. London: Taylor &
737 Francis Group, pp. 59–86.

738 Cuss, R. *et al.* (2014) 'Experimental observations of mechanical dilation at the onset of gas flow in Callovo-
739 Oxfordian claystone', *Clays in Natural and Engineered Barriers for Radioactive Waste Confinament. Geological Society,*
740 *London, Special Publications*, 400(iii), pp. 507–519. doi: 10.1144/SP400.26.

741 Dvorkin, J. *et al.* (1999) 'Elasticity of marine sediments: Rock physics modeling', *Geophysical Research Letters*,
742 26(12), pp. 1781–1784.

743 Egermann, P. and Vizika, O. (2000) 'A NEW METHOD TO DETERMINE CRITICAL GAS SATURATION AND RELATIVE
744 PERMEABILITY DURING DEPRESSURIZATION IN THE NEAR-WELLBORE REGION', in *SPE annual technical conference and*
745 *exhibition*. Society of Petroleum Engineers, pp. 1–12. doi: doi:10.2118/63149-MS.

746 Esrig, M. I. and Kirby, R. C. (1977) 'Implications of gas content for predicting the stability of submarine slopes',
747 *Marine Geotechnology*, 2(1–4), pp. 81–100. doi: 10.1080/10641197709379771.

748 Feng, T. W. (2000) 'Fall-cone penetration and water content relationship of clays', *Geotechnique*, 50(2), pp.
749 181–187. doi: https://doi.org/10.1680/geot.2000.50.2.181.

750 Grozic, J. L. H., Nadim, F. and Kvalstad, T. J. (2005) 'On the undrained shear strength of gassy clays', *Computer*
751 *and Geotechnics*, 32, pp. 483–490. doi: 10.1016/j.compgeo.2005.10.002.

752 Grozic, J. L. H., Robertson, P. K. and Morgenstern, N. R. (2000) 'Cyclic liquefaction of loose gassy sand',
753 *Canadian Geotechnical Journal*, 37, pp. 843–856.

754 Helgerud, M. B. *et al.* (1999) 'Elastic-wave velocity in marine sediments with gas hydrates: Effective medium
755 modeling', *Geophysical Research Letters*, 26(13), pp. 2021–2024.

756 Hight, D. W., Hamza, M. M. and El Sayed, A. S. (2002) 'Engineering characterization of the Nile Delta clays', in
757 Nakase, A. and Tsuchida, T. (eds) *Coastal geotechnical engineering in practice*. Lisse, the Netherlands: Swets &
758 Zeitlinger, pp. 149–162.

759 Hight, D. W. and Leroueil, S. (2003) 'Characterisation of soils for engineering purposes', in Tan, T. S. et al. (eds)
760 *Characterisation and engineering properties of natural soils - volume 1*. Lisse, The Netherlands: Swets & Zeitlinger, pp.
761 255–360.

762 Hong, Y. *et al.* (2017) 'Effect of initial pore pressure on undrained shear behaviour of fine-grained gassy soil',
763 *Canadian Geotechnical Journal*, 54(11), pp. 1592–1600.

764 Huang, T. H., Chang, C. S. and Yang, Z. Y. (1995) 'Elastic Moduli for Fractured Rock Mass', *Rock Mechanics and*
765 *Rock Engineering*, 28(3), pp. 135–144.

766 Jain, A. K. and Juanes, R. (2009) 'Preferential Mode of gas invasion in sediments : Grain-scale mechanistic
767 model of coupled multiphase fluid flow and sediment mechanics', 114(1), pp. 1–19. doi: 10.1029/2008JB006002.

768 Jang, J. and Santamarina, J. C. (2014) 'Evolution of gas saturation and relative permeability during gas
769 production from hydrate-bearing sediments: Gas invasion vs. gas nucleation', *Journal of Geophysical Research: Solid*
770 *Earth*, 119, pp. 116–126. doi: 10.1002/2013JB010480.Received.

771 Judd, A. G. and Hovland, M. (2007) 'Seabed fluid flow: the impact of geology, biology and the marine
772 environment', *Cambridge University Press*, (February), pp. 1–442. doi: 10.1007/s00254-004-1086-0.

773 Kahraman, S. (2002) 'The effects of fracture roughness on P -wave velocity', 63, pp. 347–350.

774 Katsman, R. (2015) 'Correlation of shape and size of methane bubbles in fine-grained muddy aquatic sediments
775 with sediment fracture toughness', *Journal of Structural Geology*. Elsevier Ltd, 70, pp. 56–64. doi:
776 10.1016/j.jsg.2014.11.002.

777 Kirkham, C. B. (2015) 'A 3D seismic interpretation of mud volcanoes within the western slope of the Nile Cone'.
778 Cardiff University.

779 Kopf, A. J. (2002) 'Significance of mud volcanism', *Reviews of Geophysics*, 40(2), p. 1005. doi:
780 10.1029/2000RG000093.

781 Lee, M. W. and Collett, T. S. (2006) 'Gas hydrate and free gas saturations estimated from velocity logs on
782 hydrate ridge, Offshore Oregon, USA', in Tréhu, A. M. et al. (eds) *Proceedings of the Ocean Drilling Program, Scientific*
783 *Results*. College Station, Texas: Ocean Drilling Program, pp. 1–25. doi: doi:10.2973/odp.proc.sr.204.103.2006.

784 Leucci, G. and Giorgi, L. De (2006) 'Experimental studies on the effects of fracture on the P and S wave velocity
785 propagation in sedimentary rock (" Calcarenite del Salento ")', 84, pp. 130–142. doi: 10.1016/j.enggeo.2005.12.004.

786 Liu, K., Xue, J. and Yang, M. (2016) 'Deformation behaviour of geotechnical materials with gas bubbles and
787 time dependent compressible organic matter', *Engineering Geology*. Elsevier B.V., 213, pp. 98–106. doi:
788 10.1016/j.enggeo.2016.09.003.

789 Lunne, T. *et al.* (2001) 'Deepwater sample disturbance due to stress relief', in *Proceedings of the 1st Annual*
790 *Offshore Technology Conference*. Houston, Texas, pp. 64–85.

Lunne, T. (2010) 'The CPT in offshore soil investigations - a historic perspective', (May).

Mazzini, A. and Etiope, G. (2017) 'Mud volcanism: An updated review', *Earth-Science Reviews*. Elsevier B.V., 168, pp. 81–112. doi: 10.1016/j.earscirev.2017.03.001.

Mazzini, A., Etiope, G. and Svensen, H. (2012) 'A new hydrothermal scenario for the 2006 Lusi eruption, Indonesia. Insights from gas geochemistry', *Earth and Planetary Science Letters*. Elsevier B.V., 317–318(May 2006), pp. 305–318. doi: 10.1016/j.epsl.2011.11.016.

Morgan, E. C. *et al.* (2012) 'Estimation of free gas saturation from seismic reflection surveys by the genetic algorithm inversion of a P-wave attenuation model', 77(4).

Nageswaran, S. (1983) 'Effect of gas bubbles on sediment behavior'. University of Oxford.

Nava Castro, R. *et al.* (2013) 'Variation of Mechanical Properties of Soft Marine Clay with Methane Gas Content - OMAE2013-10800', in *Proceedings of the ASME 2013 32nd International Conference on Ocean, Offshore and Arctic Engineering - OMAE2013*. Nantes, pp. 1–9.

Naylor, P. *et al.* (2000) 'Relative permeability measurements for post-waterflood depressurisation of the Miller field, North Sea', in *SPE annual technical conference and exhibition*. Dallas, Texas: Society of Petroleum Engineers, pp. 491–497.

Olsen, H. W. (1960) 'Hydraulic Flow Through Saturated Clays', *Clays and Clay Minerals*, 9(1), pp. 131–161.

Popp, T. and Salzer, K. (2007) 'Anisotropy of seismic and mechanical properties of Opalinus clay during triaxial deformation in a multi-anvil apparatus', *Physics and Chemistry of the Earth*, 32, pp. 879–888. doi: 10.1016/j.pce.2006.04.022.

Rebata-Landa, V., Santamarina, J. C. and Asce, M. (2012) 'Mechanical Effects of Biogenic Nitrogen Gas Bubbles in Soils', (February), pp. 128–137. doi: 10.1061/(ASCE)GT.1943-5606.0000571.

Revil, A. *et al.* (1998) 'Capillary sealing in sedimentary basins: A clear field example', *Geophysical Research Letters*, 25(3), pp. 389–392.

Riboulot, V. *et al.* (2013) 'Sea-level change and free gas occurrence influencing a submarine landslide and pockmark formation and distribution in deepwater Nigeria', *Earth and Planetary Science Letters*. Elsevier, 375, pp. 78–

816 91. doi: 10.1016/j.epsl.2013.05.013.

817 Ryzak, M. and Bieganowski, A. (2011) 'Methodological aspects of determining soil particle-size distribution
818 using the laser diffraction method', *Journal of Plant Nutrition and Soil Science*, 174(4), pp. 624–633. doi:
819 10.1002/jpln.201000255.

820 Shin, H. and Santamarina, J. C. (2011) 'Open-mode discontinuities in soils', *Géotechnique Letters*, 1, pp. 95–99.
821 doi: http://dx.doi.org/10.1680/geolett.11.00014.

822 Sills, G. C. *et al.* (1991) 'Behaviour of offshore soils containing gas bubbles', *Géotechnique*, 41(2), pp. 227–241.

823 Sills, G. C. Ã. and Gonzalez, R. Ã. (2001) 'Consolidation of naturally gassy soft soil', *Géotechnique*, 51(7).

824 Skempton, A. W. (1944) 'Notes on the compressibility of clays', *Quarterly Journal of the Geological Society of*
825 *London*, 100, pp. 119–135.

826 Sobkowicz, J. C. and Morgenstern, N. R. (1984) 'The undrained equilibrium behaviour of gassy sediments',
827 *Canadian Geotechnical Journal*, 21, pp. 439–448.

828 Stewart, S. A. and Davies, R. J. (2006) 'Structure and emplacement of mud volcano systems in the South
829 Caspian Basin', *AAPG Bulletin*, 90(5), pp. 771–786. doi: 10.1306/11220505045.

830 Sultan, N. *et al.* (2004) 'Triggering mechanisms of slope instability processes and sediment failures on
831 continental margins: A geotechnical approach', *Marine Geology*, 213(1–4), pp. 291–321. doi:
832 10.1016/j.margeo.2004.10.011.

833 Sultan, N. and Garziglia, S. (2014) 'Mechanical behaviour of gas-charged fine sediments: model formulation
834 and calibration', *Géotechnique*, 64(11), pp. 851–864. doi: 10.1680/geot.13.P.125.

835 Sultan, N., De Gennaro, V. and Puech, A. (2012) 'Mechanical behaviour of gas-charged marine plastic
836 sediments', *Géotechnique*, 62(9), pp. 751–766. doi: 10.1680/geot.12.OG.002.

837 Thomas, S. D. (1987) 'The consolidation behaviour of gassy soil'. University of Oxford.

838 Tingay, M. *et al.* (2008) 'Triggering of the Lusi mud eruption: Earthquake versus drilling initiation', *Geology*,
839 36(8), pp. 639–642. doi: 10.1130/G24697A.1.

840 Tingay, M. *et al.* (2017) 'An alternative review of facts, coincidences and past and future studies of the Lusi

841 eruption', *Marine and Petroleum Geology*, (December). doi: 10.1016/j.marpetgeo.2017.12.031.

842 Tingay, M. R. P. *et al.* (2015) 'Initiation of the Lusi mudflow disaster', *Nature Geoscience*, 8(7), pp. 493–494.

843 doi: 10.1038/ngeo2472.

844 Wheeler, S. J. (1988) 'The undrained shear strength of soils containing large gas bubbles', *Géotechnique*, 38(3),

845 pp. 399–413.